Constitutive Interferon Epsilon Expression Shapes Antiviral Epithelial States in the Female Reproductive Tract and Intestine

Rebecca L. Casazza[1], Samantha Skavicus[2], David Hare[1], Kaila A. Cooley[1], Nicholas S. Heaton[2,3], Carolyn B. Coyne[1,3]

1) Duke University School of Medicine, Department of Integrative Immunobiology, Durham, NC
2) Duke University School of Medicine, Department of Microbiology and Molecular Genetics, Durham, NC
3) Duke Human Vaccine Institute, Durham, NC

*Address correspondence:
Carolyn Coyne, PhD
3130 Medical Sciences Research Building III
3 Genome Court
Durham, NC 27710
USA
carolyn.coyne@duke.edu

Abstract

Antiviral defenses at mucosal barriers are essential for preventing viral entry and systemic infection. Interferon epsilon (IFNε) is a unique type I IFN that, unlike other family members, is not induced by infection but is constitutively expressed in epithelial tissues. IFNε was initially characterized in the female reproductive tract (FRT), where it provides broad antiviral protection, but its roles outside the FRT remain poorly defined. Here, we used *Ifnε*$^{-/-}$ mice and single-cell RNA sequencing to delineate IFNε function across distinct mucosal surfaces. In the FRT, *Ifnε* expression was restricted to specific epithelial subsets, was independent of estrous stage, and maintained basal ISG expression. IFNε was also retained intracellularly in primary human FRT-derived cells. Extending these analyses to the intestine, we found that IFNε is highly expressed in villous-tip enterocytes of the small intestine *in vivo*, where it sustains inflammatory enterocyte subsets and maintains type III IFN expression. Loss of *Ifnε* depleted these subsets and rendered mice more susceptible to enteric viral infection. Together, these findings establish IFNε as a constitutively expressed, spatially restricted IFN that coordinates mucosal antiviral defenses across both reproductive and gastrointestinal epithelial tissues.

Introduction

Antiviral defenses at barrier sites are essential for preventing entry and dissemination of viruses, which could compromise tissue integrity and lead to systemic infection. In the reproductive tract, these defenses are particularly crucial given exposure to external pathogens, such as sexually transmitted viruses, and their essential role in safeguarding reproductive health and ensuring successful reproduction. Similarly, in the intestine, antiviral programs are required to control constant exposure to enteric viruses while maintaining epithelial integrity and nutrient absorption. In both tissues, robust antiviral responses are needed to preserve a balanced immune environment, minimizing the risk of infection while sustaining barrier function and overall tissue homeostasis.

Interferon epsilon (IFNε) is a type I IFN that has been described as specifically enriched in the epithelial cells of the female reproductive tract (FRT) (Bourke et al., 2022; Fung et al., 2013). Unlike other type I IFNs, IFNε is constitutively expressed and is not induced by viral infections. Despite its lack of induction by infection, IFNε plays a direct role in innate antimicrobial defense against sexually transmitted infections, including HIV, herpes simplex virus (HSV), Zika virus (ZIKV), and Chlamydia (Coldbeck-Shackley et al., 2023; Fung et al., 2013; Stifter et al., 2018). Beyond antiviral defense, IFNε exerts tumor-suppressive activity in fallopian tube epithelial cells (Marks et al., 2023) and has been implicated in pregnancy, as it is expressed in the myometrium, cervix, and chorioamniotic membranes (Miller et al., 2022). Elevated levels of IFNε in amniotic fluid during spontaneous preterm labor with intra-amniotic infection suggest a role in antimicrobial defense within the amniotic cavity. However, consistent with viral infections, IFNε expression is not enhanced by bacterial stimulation *in vitro*, indicating that alternative cellular sources may contribute to its presence during infection(Fung et al., 2013; Miller et al., 2022).

Several clues exist as to the regulation of *IFNε* expression. Analysis of the *IFNε* promoter region revealed progesterone response elements implicating hormonal modulation in its expression (Hardy et al., 2004). Consistent with this, *Ifnε* expression fluctuates in the mouse

uterus with the estrous cycle, and peaks during estrous when progesterone levels are highest (Fung et al., 2013). The transcription factor ELF3, which directly regulates the expression of genes important for maintaining the integrity and function of epithelial barriers, contributes to the control of IFNε expression in the uterus and levels fluctuate with estrous status (Fung et al., 2024). Transcription factor binding site analysis has also revealed potential regulatory sites for NF-κB, a critical mediator in immune and inflammatory responses (Hardy et al., 2004). NF-κB binding elements in the IFNε promoter suggest that this cytokine might be responsive not only to hormonal signals but also to cellular stress and inflammatory stimuli, which aligns with its role in epithelial immune defense. Indeed, treatment of cells with tumor necrosis factor-α (TNF-α) upregulates *IFNε* expression (Matsumiya et al., 2007). Taken together, these findings suggest that *IFNε* expression may be finely tuned by both hormonal and inflammatory cues, with transcription factors including NF-κB and ELF3 potentially coordinating epithelial immune readiness in response to estrous phase and/or local environmental stimuli.

In addition to antimicrobial and antitumor properties in the epithelium of the FRT, IFNε potentially plays a role in modulating the immune system. For example, *Ifnε*$^{-/-}$ mice exhibit less uterine NK cell accumulation at baseline and less activation after infection than WT mice, a phenotype which results in part from differences in cytokine secretion in *Ifnε*$^{-/-}$ macrophages/monocytes (Mayall et al., 2024). Additionally, T-, B-, and NK cells respond to recombinant IFNε *in vitro* (Stifter et al., 2018). These findings suggest that IFNε not only fortifies epithelial defenses but also plays a broader immunoregulatory role in the FRT, coordinating both innate and adaptive immune responses to maintain tissue homeostasis and readiness against infection.

Recent studies have suggested that IFNε might also play a role in inflammatory signaling outside of the FRT. In addition to epithelial cells of the FRT, *Ifnε* is expressed in the intestinal epithelium, where it helps limit inflammation and supports the intestinal regulatory T cell

52 compartment (de Geus et al., 2024). In the testes, Ifnε is expressed in the germinal epithelium in
53 spermatogenic cell, as well as in leydig cells and macrophages, where it protects against infection
54 (Wijayarathna et al., 2024). Ifnε is also constitutively expressed in human primary bronchial
55 epithelial cells, and in the intestines of bats (Deng et al., 2024; Kellner et al., 2025; Martinez-
56 Espinoza et al., 2024). In rhesus macaques, IFNε is expressed in the epithelium of the large and
57 small intestines, lung, and foreskin in addition to the female reproductive tract (Demers et al.,
58 2014). These studies highlight IFNε as a multifaceted cytokine with roles in maintaining immune
59 balance across diverse mucosal tissues, suggesting it may provide a widespread defense
60 mechanism beyond the FRT.

61 The mechanisms regulating IFNε and its contributions to antiviral defense beyond the
62 female reproductive tract (FRT) remain incompletely defined. To address this, we generated an
63 IFNε knockout (*Ifnε*$^{-/-}$) mouse using a modified intracytoplasmic gene editing via oviductal nucleic
64 acids delivery (iGONAD) approach, which enables in vivo genetic modification without embryo
65 transfer (Ohtsuka et al., 2018; Skavicus and Heaton, 2023). Consistent with a previously
66 described *Ifnε*$^{-/-}$ model (Fung et al., 2013), we confirmed that IFNε protects against intravaginal
67 herpes simplex virus-2 (HSV-2) infection. Analysis of single-cell RNA sequencing (scRNA-Seq)
68 datasets across the estrous cycle in the mouse FRT (Winkler et al., 2024) revealed that *Ifnε* is
69 expressed in tissue-specific epithelial cell clusters and is not directly regulated by the estrous
70 cycle. Instead, expression varies with fluctuations in the abundance of Ifnε-expressing epithelial
71 subsets. These populations exhibited high interferon-stimulated gene (ISG) expression, which
72 was absent in epithelial subsets lacking *Ifnε*, suggesting an autocrine mechanism of action.
73 Supporting this, scRNA-seq of uterine tissues from WT and *Ifn*$^{\varepsilon-/-}$ mice showed significant
74 reductions in ISG expression specifically within Ifnε-expressing epithelial subsets, without broader
75 transcriptional effects. In primary human FRT epithelial cells, IFNε was constitutively expressed,
76 non-inducible by pathogens, and retained intracellularly. Similarly, IFNε was constitutively
77 expressed and retained intracellularly in human stem cell-derived enteroids. Single-cell RNA

sequencing of human enteroids and murine small intestine identified IFNε expression specifically in mature villous-tip enterocytes, establishing that IFNε is constitutively expressed within this epithelial subset *in vivo*. Mice lacking *Ifnε* exhibited reduced expression of antimicrobial genes, loss of inflammatory enterocyte populations that normally produce cytokines such as Ifnλ3, and increased susceptibility to oral infection with the enterovirus coxsackievirus B (CVB). These findings establish IFNε as a key contributor to mucosal immunity, sustaining antiviral defenses within tissue-specific epithelial cells of both the FRT and intestine, and broaden our understanding of its role beyond traditional pathogen-induced interferon responses.

Results

Generation of *Ifnε*$^{-/-}$ mice using iGONAD

We used a modified iGONAD protocol (Skavicus and Heaton, 2023) to generate an *Ifnε*$^{-/-}$ knockout mouse. The iGONAD technique was chosen for its efficiency and precision in gene editing, particularly in the context of creating knockout models. To achieve this, we employed a dual sgRNA approach targeting the single coding exon of the *Ifnε* gene, which resulted in a 263 basepair deletion (**Figure 1A).** Fifteen total pups were born following the injection and electroporation of sgRNAs and Cas9 into the oviducts of pregnant dams. These pups were subsequently screened for *Ifnε* knockout by PCR using primers spanning both gRNA target sites. The genotyping results revealed that 6 out of the 15 pups were homozygous for the *Ifnε* deletion, indicating a successful knockout of both alleles. Additionally, 3 pups were identified as heterozygous, carrying one wildtype and one knockout allele, while the remaining 6 pups were wildtype (representative genotypes, **Figure 1B**). Successful gene knockout was further validated by Sanger sequencing, which confirmed the deletion at the nucleotide level (**Figure Supplemental 1A**). Following this, a qPCR-based genotyping assay was developed in collaboration with a commercial vendor (Transnetyx) to streamline the genotyping process for subsequent generations. To establish a stable knockout line one animal (15) identified as

104 homozygous for the *Ifnε* deletion was selected as the founding sire. To ensure genetic integrity
105 and minimize potential off-target effects, this animal was backcrossed ~6 times with C57Bl/6J
106 mice. Following backcrossing, a stable and reproducible *Ifnε*$^{-/-}$ line was developed and used for
107 subsequent studies.

108 To confirm that this newly established *Ifnε*$^{-/-}$ line recapitulated phenotypes observed in a
109 previous *in vivo* model (Fung et al., 2013) regarding the role of IFNε in antiviral signaling in the
110 FRT, we infected *Ifnε*$^{-/-}$ and WT female mice intravaginally with 100PFU of HSV-2 (strain 333) and
111 scored mice daily for clinical signs. *Ifnε*$^{-/-}$ mice lost more weight compared to their WT counterparts
112 (**Figure 1C, 1D**), a higher percentage of *Ifnε*$^{-/-}$ mice succumbed to infection (73% vs 40%),
113 (**Figure 1E**) a higher percentage of *Ifnε*$^{-/-}$ mice had disease onset compared to WT mice (89% vs
114 60%), defined as any observable clinical sign, (**Figure 1F**) *Ifnε*$^{-/-}$ mice displayed higher frequencies
115 of advanced clinical signs throughout the course of infection (**Figure 1G, 1H**). Despite *Ifnε*$^{-/-}$ having
116 worse disease outcomes by every metric measured, none of these differences were significant,
117 in part due to a large proportion of mice that remained uninfected. To increase infection rates in
118 our mice, we performed infections with 10,000PFU of HSV-2 (**Figure 1I, 1J).** *Ifnε*$^{-/-}$ had higher viral
119 burdens in vaginal lavages at 2 and 3dpi (**Figure 1I**) and had worse clinical outcomes measured
120 by clinical scores (median of 3 in WT mice vs median of 6 in *Ifnε*$^{-/-}$ mice, $p = 0.0741$ measured by
121 Mann Whitney) (**Figure 1J**). Taken together, these data show that *Ifnε*$^{-/-}$ mice generated using
122 iGONAD recapitulate the heightened susceptibility and impaired antiviral response observed in a
123 previous *in vivo* model of HSV-2 infection in the FRT.

124

125 **IFNε is a Key Modulator of Basal ISG Expression in the FRT Epithelium**

126 To determine the specific cell types expressing *Ifnε* in the uterus and the functional consequences
127 of *Ifnε* signaling, we performed scRNASeq on uterine tissue isolated from WT and *Ifnε*$^{-/-}$ mice in
128 estrous, with 19227 cells passing quality control. Cluster analysis and cell-type specific marker
129 expression following integration to correct for batch effects across independent animals revealed

130 four distinct clusters of EpCs, two populations of endothelial cells (Endo), stroma and fibroblasts,
131 two populations of muscle cells (Musc-1 and Musc-2), pericytes (Peri), and various immune cells
132 including macrophages (Mac), dendritic cells (DC), and NK cells (NK) (**Figure 2A**). There were
133 near-equivalent ratios of all cell types between WT and *Ifnε*$^{-/-}$ mice (**Figure 2B, Supplemental**
134 **Figure 2A**) and cell clusters expressed cell type-specific markers, which were conserved between
135 WT and *Ifnε*$^{-/-}$ mice (**Figure 2C**, **Supplemental Figure 2B**). We identified a single cluster of EpCs
136 (EpC-2) that highly expressed *Ifnε* and that also expressed high basal ISG levels (**Figure 4D**).
137 This cluster also expressed markers associated with LEpCs (e.g., *Prap1*, *Tacstd2*, *Ltf*)
138 (**Supplemental Figure 2C**, **2D**).

139 To assess whether *Ifnε* expression was required for basal ISG expression in EpC-2 and
140 other cell types, we performed pseudobulk differential expression analysis across all cell clusters
141 in WT and *Ifnε*$^{-/-}$ mice. We identified a total of 115 differentially downregulated transcripts in
142 *Ifnε*$^{-/-}$ mice compared to WT, with ~70% of these differentially expressed genes (DEGs) attributed
143 specifically to the EpC-2 cluster (**Supplemental Figure 2E**). Pathway analysis of these DEGs
144 showed a significant enrichment in genes associated with IFN signaling and the antiviral response
145 (**Figure 2E**). Of the 81 differentially downregulated DEGs in EpC-2, ~45% of them were ISGs
146 (**Figure 2F).** Several additional clusters also exhibited a downregulation of select ISGs (EpC-3,
147 EpC-4, Stroma, and DC), but the total number of DEGs was significantly lower than that observed
148 in EpC-2 (**Figure 2F**). Additional clusters, including EpC-1, Endo-2, Fib, and Musc-1 did not
149 exhibit any changes in gene expression in *Ifnε*$^{-/-}$ mice (**Figure 2F**). There were only two DEGs
150 enriched in *Ifnε*$^{-/-}$ mice, *Ppbp* and *Crct.* Importantly, although ISGs were significantly
151 downregulated in EpC-2, other non-IFN-mediated inflammatory transcripts were unchanged,
152 including those associated with IL1 signaling (e.g., *Il1a*), chemokine signaling (e.g., *Cx3cl1*), and
153 cytokine signaling (e.g., *Mif*) (**Figure 2G-2I**). Taken together, these data show that *Ifnε* expression
154 is crucial for maintaining basal ISG expression in EpC populations in the FRT.
155

156 ***Ifnε* is expressed in epithelial cells of the oviduct, uterus, cervix, and vagina independent**
157 **of estrous status**

158 To determine to determine the impact of the estrous cycle on the expression of *IFNε* in the
159 FRT, we analyzed an existing single cell atlas of the cycling mouse female reproductive tract
160 based on 378,516 cells from normal cycling young mice in the four cycle phases (proestrus [Pro],
161 estrus [Est], metestrus [Met], and diestrus [Di]) (Winkler et al., 2024). The dataset contained cells
162 harvested from ovary, oviduct, uterus, cervix, and vagina from 3-5 independent animals. We
163 restricted our analyses to non-pregnant young mice (aged <12 months). A total of 71173 (Ovary),
164 75091 (Oviduct), 49889 (Uterus), 78967 (Cervix), and 82861 (Vagina) cells passed quality control
165 and were used for cluster analysis and cell-type specific marker expression analysis following
166 integration to correct for batch effects (**Figure 3A, Figure S3A-J**). We broadly clustered cells into
167 epithelial cells (EpC), stromal cells, immune cells, endothelial cells (EndoC), or muscle cells. Each
168 tissue site exhibited site-specific enrichment of these cell types, consistent with what has been
169 described (Winkler et al., 2024), with the cervix and vagina most enriched in EpCs and ovary,
170 oviduct, and uterus more enriched in stromal cells (**Figure 3A**, **Figure S3A-J**). While there was
171 slight variation in the proportion of these cell types during the estrous cycle, including the
172 enrichment of immune cell types in the cervix and vagina during Met, the proportion of cell types
173 were largely maintained across all tissues (**Figure 3B**).

174 We next determined the cell type(s) expressing *Ifnε* across all tissue sites and defined the
175 impact of the estrous cycle on this expression. For this analysis, we further clustered cell types to
176 increase resolution. In the oviduct, uterus, cervix, and vagina, we found that *Ifnε* was specifically
177 enriched in EpC cell types that also expressed high levels of epithelial markers (e.g., *Cdh1*,
178 *EpCam*) (**Figure 3C**). We did not detect any *Ifnε* in the ovaries (**Figure 3C**). We next determined
179 the levels of *Ifnε* expressed in EpCs across the estrous cycle in all tissues. In the oviduct, cervix,
180 and vagina, we observed highly similar levels of expression across all stages of the estrous cycle
181 (**Figure 3D**). In the uterus, levels of *Ifnε* were consistent across Pro, Est, and Di, with significantly

182 lower levels in Met (**Figure 3D**). Similarly, *Ifnε* levels were low in the uterus of pregnant mice
183 (**Figure S3K, S3L**). Taken together, these data indicate that IFNε is predominantly expressed in
184 epithelial cell types across the FRT, with consistent expression levels across the estrous cycle,
185 except in the uterus where levels significantly decrease during Met and pregnancy.
186

187 ***Ifnε*-expressing epithelial cells in the FRT express high basal ISGs**

188 The FRT is lined by specialized epithelial cell types, each with distinct functions tailored to their
189 anatomical location. These include ciliated and secretory EpCs in the oviduct, luminal and
190 glandular EpCs in the uterus, mucus-secreting EpCs in the cervix, and stratified squamous EpCs
191 in the vagina. Given that *Ifnε* was expressed in EpC populations across the FRT, we next sought
192 to identify the specific EpC populations responsible for this expression and whether it varied by
193 location. Furthermore, we sought to investigate whether *Ifnε*-expressing epithelial cell populations
194 exhibited distinct transcriptional profiles, including elevated ISG levels. To do this, we subsetted
195 the EpC cell cluster from all anatomical sites and re-clustered to obtain better resolution between
196 distinct EpC types. In the oviduct, EpC cells were clustered into ciliated (cEpC) and secretory
197 (SEpC) populations, which were distinguished based upon marker expression (**Supplemental**
198 **Figure 3A-3B**). We found that *Ifnε* was specifically expressed in an SEpC cell population marked
199 by *Serpina1e* expression (**Supplemental Figure 3C, 3D**). This population also exhibited high
200 basal levels of ISGs (**Supplemental Figure 3C**). In the uterus, EpCs were distinguished between
201 markers associated with luminal EpCs (LEpCs) and glandular EpCs (GlEpCs) (**Supplemental**
202 **Figure 3E**), with *Ifnε* expression restricted to a LEpC population expressing high levels of Tactstd2
203 (**Supplemental Figure 3F-3H**). This cluster also expressed high levels of diverse ISGs
204 (**Supplemental Figure 3G**). The cervix contained the largest number of EpCs, which sub-
205 clustered into intermediate (IEpCs), superficial (SuEpCs), and basal EpCs (BEpC), some of which
206 were proliferating (pBEpC) (**Supplemental Figure 3I, 3J**). *Ifnε* was expressed in both SuEpC
207 populations, with significantly higher levels in the Sprr2d^{+} cluster, which also showed elevated

ISG expression (**Supplemental Figure 3K, 3L**). The vaginal EpCs clustered into SuEpCs, BEpCs, and columnar EpCs (ColEpCs), with ColEpCs expressing both *Ifnε* and basal ISGs (**Supplemental Figure 3M-3P**). These data demonstrate that *Ifnε* is expressed in specific epithelial cell populations across tissue sites, with its expression correlating with high basal levels of ISG expression within these clusters.

The data described above suggested that *Ifnε* is expressed in distinct EpC types in an anatomical location-specific manner, suggesting that these cell types might exhibit conserved expression of factors responsible for *Ifnε* expression. To determine if this was the case, we compared the differentially enriched genes in all *Ifnε* expressing clusters across anatomical sites and identified the genes shared between these cell types. This analysis revelated that only 31 genes (1% of the total genes) were shared between *Ifnε* expressing EpC types (**Supplemental Figure 5A**). The top-most gene shared across all cell clusters was *Elf3* (**Supplemental Figure 5B**), which has been shown previously to regulate *Ifnε* expression (Fung et al., 2024). In fact, there were only two transcription factors shared between all *Ifnε*-expressing EpC clusters, which included *Elf3* and *Maff* (**Supplemental Figure 5C**). These findings suggest that, despite the anatomical specificity of *Ifnε* expression, only a small set of conserved transcription factors, which included *Elf3*, may play a role in regulating *Ifnε* expression across diverse epithelial cell types.

IFNε is retained intracellularly and is not induced by viral infections in primary human epithelial cells

To assess whether IFNε expression levels changed following infection, we cultured human primary endometrial and vaginal epithelial cells, infected them with Sendai virus (SeV) or HSV-2, or treated them with a variety of PAMPs including poly(I:C), cGAMP, and LPS, and measured *IFNε* expression by qRT-PCR. Consistent with what we observed in the mouse scRNAseq analysis described above, *IFNε* was basally expressed in both uterine and vaginal primary cells and expression levels were unchanged with infection or PAMP treatment (**Figure 4A, 4B)**. In

contrast, *IFNβ* was undetected at baseline, and was induced by all conditions except for LPS treatment (**Figure 4A, 4B).** To broadly profile the induction of *IFNε* and other IFNs, we performed whole transcriptome bulk RNA-Seq on uterine and vaginal epithelial cells infected with SeV, as well as on mock-infected controls. Both cell types responded to infection by induction of various IFNs, including *IFNβ* and *IFN*λ 1-3, as well as canonical ISGs (e.g., *OAS1*, *OASL*, *ISG15*) (**Figure 4C-4E**). In contrast, although *IFNε* was expressed basally, it was not induced by SeV infection in either cell type (**Figure 4D**, **4E**).

In our scRNAseq datasets, we observed basal ISG expression in clusters that also expressed *Ifnε*, suggesting an autocrine role for IFNε signaling in subsets of epithelial cells of the FRT. To determine if IFNε is retained intracellularly, we examined both lysates and supernatants from human uterine and vaginal primary epithelial cells for IFNε or IFNβ levels by ELISA. IFNε was undetectable in the supernatants from vaginal and uterine primary cells basally, after poly(I:C) treatment, and after SeV infection (**Figure 4F, 4G**). However, there were high levels of IFNε detected in the cell lysates in all conditions, although there was significantly more IFNε at baseline than there was following poly(I:C) treatment or infection (**Figure 4F, 4G).** In contrast, IFNβ was undetectable at baseline and although it could be observed at low levels in cell lysates following poly(I:C) treatment or SeV infection, it was significantly higher in the supernatants **(Figure 4H, 4I).** Together, these data indicate that IFNε is constitutively expressed and retained intracellularly within epithelial cells of the FRT, where it likely functions through autocrine signaling, in contrast to IFNβ, which is secreted in response to infection.

IFNε is basally expressed in and retained intracellularly in human intestinal organoids

IFNε has been reported to be expressed in the gastrointestinal tract and may be associated with colitis (de Geus et al., 2024). To determine if IFNε is retained intracellularly in the gastrointestinal tract as well as in the FRT, we examined cells and supernatants of human stem-cell derived enteroids. To include diverse GI cell types, human enteroids were grown in expansion media (Exp)

260 to maintain a proliferative state with stem and progenitor cells or under differentiation conditions
261 (Dif) to promote their maturation into specialized cells, including enterocytes, goblet cells, and
262 Paneth cells (Fujii et al., 2018; He et al., 2022). Consistent with the FRT epithelium, IFNε was
263 undetectable in the supernatants of both Exp and Dif enteroids and was only detected by ELISA
264 in the cell lysates of both culture conditions (**Figure 5A**)**.** To define the expression of IFNε in the
265 GI tract we performed scRNASeq of intestinal organoids under differentiation and expansion
266 conditions. Enteroids cultured under these conditions contained $CD24^+$ progenitor cells, transit
267 amplifying cells, immature enterocytes, mature enterocytes, $BEST4^+$ ionocytes, goblet cells, and
268 enteroendocrine cells, which expressed canonical markers associated with these cell types
269 (**Figure 5B-5D**). As expected, we found that Exp enteroids were enriched in $CD24^+$ cells, transit
270 amplifying cells, and immature enterocytes and Dif enteroids were enriched in mature
271 enterocytes, and $BEST4^+$ ionocytes and exhibited differences in cell type-specific expression
272 (**Figure 5C, Supplemental Figure 6A, 6B**). We found that *IFNε* was enriched in both mature
273 enterocyte populations, as well as in a population of immature enterocytes (**Figure 5D,**
274 **Supplemental Figure 6C**). The only other IFN detectable in the dataset was *IFNκ*, which was
275 expressed at very low levels in $CD24^+$ cells (**Figure 5D**).
276

277 **IFNε is expressed in proximal, villus-tip enterocytes in the small intestine**

278 To define the cellular expression patterns of *Ifnε* in the small intestine and assess its role
279 in regulating ISG expression in the GI tract, we performed scRNA-seq on whole small intestines
280 from WT and *Ifnε*$^{-/-}$ mice. All samples were merged and integrated together to correct for batch
281 effects and to ensure identification of cell types across experimental conditions, with 93,309 cells
282 passing quality control. Clustering identified 23 unique clusters (**Figure 6A).** All clusters were
283 present across all samples and there were similar proportions of each cluster in WT and *Ifnε*$^{-/-}$
284 samples **(Supplemental Figure 7A, 6B).** Clusters were annotated based on the expression of
285 conserved marker genes, identifying major epithelial lineages (enterocytes, Paneth cells, goblet

286 cells, tuft cells, enteroendocrine cells, and stem cells), as well as immune (T and B cells) and
287 mesodermal populations **(Figure 6B).** Consistent with our observations in enteroids, we observed
288 that *Ifnε* expression *in vivo* was primarily restricted to enterocyte populations, with Enterocyte
289 cluster 2 (Ent2) exhibiting the highest proportion of *Ifnε* positive cells **(Figure 6C, 6D).** Because
290 only ~10% of cells within Ent2 expressed *Ifnε*, we subsetted this cluster and performed
291 reclustering to resolve enterocyte subpopulations and more precisely define the epithelial subset
292 responsible for *Ifnε* expression (**Figure 6E).** Reclustering resolved 7 transcriptionally distinct
293 enterocyte subpopulations, among which Ent2-D showed the highest *Ifnε* expression, with 60%
294 of cells expressing the gene (**Figure 6F).** Ent2-D was marked by expression of duodenal
295 cytochrome B (*Cybrd1*), a ferric reductase that is expressed in the brush border of duodenal
296 enterocytes (McKie et al., 2001), as well as *Nt5e*, which is associated with villous tips (Moor et
297 al., 2018) **(Figure 6G)**. These features indicate that *Ifnε* expression is enriched in proximal small
298 intestinal enterocytes at the villous tips. To investigate this further, we calculated a villous index
299 score for each cell type in the intestinal dataset, defined as the ratio of villous tip-associated genes
300 to the sum of villous tip- and villous bottom-associated genes, as described previously (Moor et
301 al., 2018). The *Ifnε*-expressing subset of Ent2 displayed relatively high villous index scores,
302 indicating enrichment in enterocytes positioned near the villous tips **(Supplemental Figure 7C).**
303 This localization is consistent with previous observations that *Ifnε* is preferentially expressed in
304 epithelial cells situated closest to the luminal surface of the colon (de Geus et al., 2024). To assess
305 whether *Ifnε*-expressing cells also exhibit elevated ISG levels, we performed a correlation analysis
306 between *Ifnε* and all other genes within the subsetted Ent2 dataset (**Figure 6H**). No significant
307 correlations were observed between *Ifnε* and ISGs, suggesting that *Ifnε* may serve functions in
308 the small intestine distinct from basal antiviral gene induction. Instead, the top genes positively
309 correlated with *Ifnε* included *Syt8*, *Cldn4*, *Add2*, and *Mucl3*, markers associated with villous tip
310 enterocytes (**Figure 6H–I**).

311 **Loss of *Ifnε* depletes inflammatory enterocyte subsets and increases susceptibility to**
312 **enteric viral infection**

313 To determine the broader impact of loss of *Ifnε* expression on intestinal homeostasis, we
314 compared the small intestinal transcriptomes of WT and *Ifnε*$^{-/-}$ mice. Using pseudobulk differential
315 expression analysis across all clusters in the dataset, we identified genes differentially expressed
316 between genotypes (**Figure 7A).** DEGs were most abundant in enterocyte clusters, where they
317 were enriched in pathways involved in antimicrobial and immune responses **(Figure 7B).** Notably,
318 genes such as *Reg3g* (antimicrobial lectin), *Nos2* (nitric oxide synthase), *Tifa* (NF-κB signaling
319 adaptor), and *Alpk1* (innate immune kinase) were differentially expressed across multiple
320 enterocyte subsets **Figure 7C, Supplemental Figure 8A, 8B).** To further resolve enterocyte
321 heterogeneity, we subsetted and reclustered Ent1-8, excluding Ent9, which was defined by
322 mitochondrial gene expression and likely represented dying cells. This analysis revealed a distinct
323 population of inflammatory enterocytes (NFκB^{Ent}) present in WT intestines but largely absent from
324 *Ifnε*$^{-/-}$ samples (**Figure 7D–E**). The NFκB^{Ent} cluster was characterized by expression of *Nfkbia*
325 (encoding an NFκB inhibitor), the NFκB regulator *Ubd*, and multiple inflammatory mediators,
326 including *Nos2*, *Ccl20*, and *Cxcl11* (**Figure 7G**). Although NFκB^{Ent} cells did not express *Ifnε*, they
327 were the only enterocyte subset to express *Ifnλ3*, the gene encoding a member of the type III IFN
328 family (**Figure 7G**). *Ifnκ* was the only other IFN detected in enterocytes, but it was not expressed
329 in NFκB^{Ent} cells. Strikingly, *Ifnλ3* expression was readily detected in WT enterocytes yet was
330 completely absent in *Ifnε*$^{-/-}$ samples, suggesting that *Ifnε* may be involved in maintaining Ifnλ
331 expression in the intestinal epithelium.

332 As Ifnλ is a central mediator of antiviral protection in the GI tract (Lazear et al., 2019), we
333 next tested whether *Ifnε*$^{-/-}$ mice were more susceptible to enteric viral infection. To test this, we
334 infected WT and *Ifnε*$^{-/-}$ mice with coxsackievirus B (CVB), an enterovirus that infects via the enteral
335 route. Mice were infected with CVB3 (H3) by oral gavage. *Ifnε*$^{-/-}$ mice exhibited significantly greater
336 weight loss than WT controls (**Figure 7I**) and showed increased mortality following infection

(**Figure 7J**). Notably, viral burdens in secondary organs, including the heart, liver, pancreas, and brain, sites commonly affected by CVB, were markedly elevated in *Ifnε*$^{-/-}$ mice relative to WT controls (**Figure 7K**). To confirm that these differences were not due to microbiome alterations in WT or *Ifnε*$^{-/-}$ mice, which have been shown to impact CVB infection (Robinson et al., 2019), we conducted 16S rRNA sequencing of the small ribosomal subunit from fecal samples of *Ifnε*$^{+/-}$ and *Ifnε*$^{-/-}$ littermates, thereby controlling for potential cage effects. The resulting dataset contained 2,695 OTUs, excluding those with a total count below three. On average, 76,503 quality-filtered reads were generated per sample, ensuring a robust analysis of microbiome composition (**Supplemental Figure 9A)**. High-quality reads were classified using the Silva v. 138 reference database, and OTUs were aggregated at each taxonomic rank (**Supplemental Figure 9B**). Alpha diversity, measured by the Shannon index, was comparable between *Ifnε*$^{-/-}$ (mean = 4.004, SD = 0.015) and WT (mean = 3.865, SD = 0.262) mice (**Supplemental Figure 9C)**. Differential abundance testing using DESeq2 revealed no OTUs with statistically significant differential abundance between WT and *Ifnε*$^{-/-}$ mice, indicating that microbiome composition was similar across genotypes. Together, these findings indicate that *Ifnε* protects against enteric viral infection, thereby acting as a critical barrier that prevents systemic viral dissemination from the gastrointestinal tract.

Discussion

Antiviral defenses at mucosal surfaces are a crucial first-line defense against systemic infection. Type I IFNs play well-established roles in mucosal immunity and are induced by infection to elicit antiviral programs in target cells by signaling through the type I IFN receptor. Although IFNε is a type I IFN that also signals through the type I IFN receptor, it is not induced by infection or PAMPs. IFNε was initially characterized in the epithelium of the FRT where it was proposed to be hormonally regulated, and more recently in the epithelium of the colon, indicating that IFNε has a role in immunity across many epithelial barriers. Here, we demonstrate that IFNε plays a

363 constitutive, essential role in antiviral defenses across mucosal sites. Using an *Ifnε*$^{-/-}$ mouse
364 model, we confirmed that IFNε provides innate antiviral protection within the FRT, where it is
365 expressed in specific epithelial cell clusters in a location-dependent manner and is associated
366 with basal ISG expression independent of estrous cycle. Extending these findings to the intestine,
367 we showed that IFNε is expressed in villous-tip enterocytes of the small intestine, where it
368 supports inflammatory enterocyte subsets and sustains *Ifnλ3* expression. Loss of *Ifnε* led to
369 depletion of these subsets, impaired *Ifnλ3* expression, and heightened susceptibility to enteric
370 viral infection with systemic dissemination. Together, these results establish IFNε as a critical
371 component of mucosal immunity, providing sustained antiviral defense across both reproductive
372 and gastrointestinal epithelial tissues. Together, these results highlight IFNε as a critical
373 component of mucosal immunity, offering sustained antiviral defense across both reproductive
374 and GI epithelial tissues.

375 IFNε has been primarily studied in the context of the FRT, where it is expressed in the
376 epithelium and has direct antimicrobial and antitumor activity. Using scRNAseq, we further defined
377 the epithelial populations that express *Ifnε* throughout the mouse FRT using an existing single cell
378 atlas of normally cycling mice (Winkler et al., 2024). We found that *Ifnε* is expressed in distinct
379 epithelial cell types in each tissue: luminal and secretory cells in the uterus; columnar cells in the
380 vagina; ciliated cells in the oviducts; and superficial cells in the cervix. In each epithelial population
381 that expressed *Ifnε* we examined its expression levels at each estrous cycle stage. While *Ifnε*
382 expression showed some fluctuations with estrous stage within individual tissues, it was
383 consistently observed at all stages, with no patterns of fluctuation that were consistent across all
384 tissues. The cell types that express *Ifnε* in the uterus; secretory and luminal epithelial cells, make
385 up the layers of the endometrium that expand in preparation for embryo implantation during
386 estrous (Jin, 2019) which could result in the higher gross *Ifnε* transcripts at a tissue level that
387 others have observed in the uterus. These findings refine our understanding of *Ifnε* expression in
388 the FRT, revealing its presence in distinct epithelial populations across tissues and estrous

389 stages, suggesting a stable role in mucosal immunity that adapts to tissue-specific epithelial
390 dynamics, especially in the endometrial layers preparing for implantation.

391 Previous studies have identified a role for IFNε in modulating inflammation in colitis models
392 and shown Ifnε expression by IHC in the colon (de Geus et al., 2024). To further define the cell
393 types that express IFNε in the intestine, we analyzed *IFNε* expression in human enteroids and in
394 mouse intestinal scRNAseq data sets. We used enteroid models cultured under two separate
395 conditions to capture the spread of intestinal cell types in the intestine and found *IFNε* in mature
396 and immature enterocytes in enteroids. In mice we observed *Ifnε* primarily in enterocytes, as well
397 as in select T-cell populations. Murine enterocytes enriched for *Ifnε* also expressed markers of
398 villus-tip localization as well as a duodenal marker, indicating that *Ifnε* expression is restricted to
399 proximal villous-tip enterocytes. These epithelial cells are the ones most directly exposed to
400 luminal contents, positioning IFNε to provide front-line antiviral protection. Unlike in the FRT,
401 where Ifnε expression correlated with ISG enrichment, intestinal analyses revealed no such
402 association. Instead, *Ifnε*$^{-/-}$ mice showed loss of key antimicrobial genes, including *Nos2* and
403 *Reg3g*, across multiple enterocyte clusters. Strikingly, ~25% of enterocytes in WT mice formed
404 an immune-activated cluster characterized by expression of chemokines and *Ifnλ3* that was nearly
405 absent in *Ifnε*$^{-/-}$ mice. This reveals a previously unrecognized crosstalk between constitutive IFNε
406 and inducible type III IFNs, whereby IFNε sustains epithelial *Ifnλ* expression programs essential
407 for gut antiviral immunity. Prior studies have shown that tonic IFNλ signaling establishes a basal
408 antiviral state that restricts enteric pathogens (Van Winkle et al., 2022). Our findings suggest that
409 IFNε functions as an upstream regulator of this tonic IFNλ environment, maintaining baseline
410 antiviral readiness in the intestinal epithelium. In accordance with this, In *Ifnε*$^{-/-}$ mice we observed
411 that IFNε exhibits antiviral activity against the enteric virus coxsackievirus B (CVB) following oral
412 infection. *Ifnε*$^{-/-}$ mice exhibited increased weight loss and mortality following infection which
413 corresponded with higher viral titers in the intestines, heart and liver at 4dpi. Taken together, these

414 data define a role for IFNε throughout the intestines, where it is expressed in enterocytes and
415 controls viral infection.

416 It is possible that IFNε is expressed at other cellular barriers including the upper and lower
417 airway, blood brain barrier, urinary tract, testes and/or eyes. We initially expected that IFNε-
418 expressing cell types would share common features; however, we observed distinct anatomical
419 differences among the epithelial populations expressing *IFNε*. IFNε has been identified in tissues
420 by IHC and is often found in the epithelial cells lining the lumen of tissues (de Geus et al., 2024;
421 Demers et al., 2014; Fung et al., 2013; Marks et al., 2023). This pattern suggests that IFNε
422 expression may be influenced by specific environmental or spatial triggers within these barriers.
423 Recently, the transcription factor ELF3 was identified as driver of *Ifnε* expression in the mouse
424 uterus (Fung et al., 2024), where it appears to support tissue-specific immune readiness. ELF3 is
425 an epithelium-specific transcription factor involved in regulating the expression of genes essential
426 for barrier function and epithelial integrity. While we consistently observed *Elf3* expression almost
427 exclusively in *Ifnε*-expressing clusters throughout the FRT, in the intestine *Elf3* was detectable in
428 nearly all cell types, indicating that there are other factors that control *IFNε* expression. This
429 finding indicates that distinct transcriptional programs may regulate IFNε expression across
430 different tissues, potentially adapting its expression to localized immune needs and environmental
431 cues. Together, these observations suggest that IFNε expression is not only anatomically
432 specialized but may also be regulated by diverse transcriptional drivers in response to the unique
433 environmental contexts of each barrier tissue.

434 We focused on the direct antiviral effects of IFNε signaling in epithelial cells, but it is likely
435 that IFNε also plays a nuanced role in immune cell signaling. Many groups have reported that
436 immune cells respond to recombinant IFNε treatment by becoming activated, expanding, or
437 upregulating ISGs (de Geus et al., 2024; Garcia-Minambres et al., 2017; Marks et al., 2019). This
438 is not surprising, as type I IFNS can activate or influence virtually all immune cell types. It has
439 been observed that IFNε knockout mice have reduced NK cells numbers in the uterus, a

440 phenotype that results in part from decreases in IL-15 signaling in *Ifnε*$^{-/-}$ macrophages/monocytes
441 (Mayall et al., 2024). In mouse models of colitis, *Ifnε*$^{-/-}$ mice exhibit decreased levels of T_{regs} in the
442 intestines which exacerbates intestinal pathology (de Geus et al., 2024; Fung et al., 2013). These
443 findings indicate that IFNε likely has a role in regulating resident tissue immune cells as well as
444 those that respond during infection. In our scRNAseq data set of the mouse intestine, we
445 observed that a small portion (1-2%) of two our T-cell clusters expressed *Ifnε* and that several
446 immune cell clusters, including T-cells, had differentially expressed genes in our *Ifnε*$^{-/-}$ mice that
447 included cytokines such as *Il17a*. It remains to be determined if these differences in immune cells
448 contribute to the phenotypes we see in *Ifnε*$^{-/-}$ mice and could be addressed in future studies using
449 *Ifnε*$^{-/-}$ conditional knockouts.

450 Although many cell types respond to IFNε after exogenous treatment with recombinant
451 protein, the cellular targets of IFNε signaling have not been well-defined in models where it is
452 basally expressed. In our scRNAseq analyses of the FRT, we observed ISG expression restricted
453 to cells that also basally expressed IFNε. This ISG expression is dependent on IFNε, as *Ifnε*$^{-/-}$
454 mice lack ISG expression in the absence of IFNε signaling, suggesting an autocrine role for IFNε.
455 Moreover, in primary human vaginal and uterine epithelial cell lines, we found that IFNε was
456 detectable by ELISA in cell lysates but was undetectable in cell supernatants regardless of viral
457 infection or stimulation. We observed similar results in human enteroids, where IFNε expression
458 could be readily detected by scRNAseq and ELISAs of cellular lysates, but not in supernatants.
459 In contrast to this, we did not see any correlation between *Ifnε* and ISGs in our mouse intestine
460 scRNAseq. Moreover, we observed many differentially expressed genes in the *Ifnε*$^{-/-}$ small
461 intestine, including in cell types that did not express *Ifnε*, indicating that IFNε signaling has effects
462 that extend beyond autocrine signaling. Most notably, *Ifnε*$^{-/-}$ mice lacked entire inflammatory
463 enterocyte populations that expressed *Ifn*λ in WT mice. One explanation for this could be that
464 Ifnε is retained intracellularly and is released from enterocytes as they are shed into the lumen of
465 the intestine as part of normal epithelial turnover and intestinal homeostasis. Future studies will

466 be crucial in elucidating the precise mechanisms by which IFNε initiates signaling and identifying
467 the specific cellular contexts where its autocrine activity plays a protective role, which may provide
468 new insights into its unique function at mucosal barriers.

469 Unchecked interferon responses can lead to debilitating autoimmune diseases and post
470 infection pathology, highlighting the need for regulation of a constitutively expressed interferon.
471 Retaining IFNε intracellularly within specific epithelial layers vulnerable to infection may prevent
472 aberrant immune activation while still providing basal antiviral protection. However, in cases of
473 cellular damage or viral infection, IFNε could also function as a damage-associated molecular
474 pattern (DAMP). Upon epithelial cell damage or lysis, IFNε may be released into the extracellular
475 space, where it could act in a paracrine manner to signal neighboring mucosal cells or immune
476 cells. This release could enhance local immune responses and alert surrounding tissues to
477 infection or injury, promoting a targeted antiviral response while still limiting widespread immune
478 activation.

479 Together, our findings underscore the unique role of IFNε in maintaining mucosal immunity
480 as a constitutively expressed IFN within epithelial barriers. By providing baseline antiviral
481 protection while remaining poised for activation upon cellular damage or infection, IFNε serves as
482 both a steady immune defender and a potential DAMP, capable of alerting neighboring cells to
483 pathogenic threats. The enrichment of IFNε in villous-tip enterocytes highlights the importance of
484 spatial positioning within the intestinal epithelium, placing this IFN at an interface where viral entry
485 is most likely to occur. Moreover, the dependence of *Ifnλ3* expression on IFNε reveals a previously
486 unappreciated regulatory axis between constitutive and inducible IFNs that shapes epithelial
487 antiviral programs. This dual functionality helps prevent unwanted immune activation that could
488 lead to autoimmune pathology, while ensuring rapid and localized antiviral responses when
489 needed. Future studies aimed at clarifying the intracellular signaling mechanisms of IFNε and its
490 DAMP-like functions may reveal new therapeutic approaches for enhancing mucosal immunity
491 without triggering systemic inflammation.

492

493 **Acknowledgments**

494 This work was supported by R01AI081759 (C.B.C). N.S.H is funded in part by R01AI168107. We
495 thank the Duke University School of Medicine for the use of the Sequencing and Genomic
496 Technologies Shared Resource, which provided RNA-seq services.

497

498 **Methods**

499 **Generation of IFNε Knockout Mice Using iGONAD**

500 IFNε knockout (*Ifnε*$^{-/-}$) mice were generated using the Genome Editing via Oviductal Nucleic Acid
501 Delivery (iGONAD) technique, as previously described (Ohtsuka et al., 2018; Skavicus and
502 Heaton, 2023). Briefly, female C57BL/6J mice were mated with C57BL/6J males. On the morning
503 of day E0.7, CRISPR/Cas9-mediated gene editing was performed on pregnant mice by injecting
504 a ribonucleoprotein (RNP) complex consisting of Cas9 protein and two guide RNA (gRNAs)
505 targeting exon 1 (AACGGATTCCCTTCCAATTG[TGG] and
506 AAGTCTTAGCTGCGCTTCAC[CGG], where the PAM sites are indicated with [PAM]) of the *Ifnε*
507 gene into the oviducts. The two gRNAs were designed to flank and induce double-strand breaks,
508 leading to the deletion of a 263 basepair fragment within exon 1, which resulted in a frameshift
509 mutation and knockout of IFNε expression. After injection, the oviducts were electroporated to
510 facilitate the delivery of the ribonucleoprotein (RNP) complex into presumed one-cell stage
511 zygoyes. After gene editing surgery, embryos continued to develop, and pregnant females were
512 allowed to deliver naturally. Genotyping of the resulting pups was carried out by extracting
513 genomic DNA from toe biopsies using a lysis buffer containing 50 mM Tris-base (pH 8.0), 50 mM
514 KCl, 2.5 mM EDTA, 0.45% IGEPAL CA-630 (NP40), 0.45% Tween-20, and 20 mg/mL proteinase
515 K, followed by incubation at 94°C for 10 minutes. PCR amplification was performed with primers
516 flanking the gRNA target sites (forward: TCCCAGAACTGGAGTGGT; reverse:

517 AAGAGCCAACAGGGGATTT) using TITANIUM Taq DNA Polymerase (Takara). The knockout was
518 further confirmed by Sanger sequencing using a primer upstream of the gRNA sites
519 (TCCCAGAACTGGAGTGGT) to verify successful deletion of the *Ifnε* gene. Ifnε$^{-/-}$ mice were
520 backcrossed to C57BL/6J for at least six generations before use in experiments to establish a
521 stable knockout line. Once established, Transnetyx developed a custom qPCR-based genotyping
522 assay to streamline the identification of *Ifnε* knockout alleles in subsequent generations.
523

524 **Viruses**

525 HSV-2 (strain 333) was provided by Helen Lazear (University of North Carolina at Chapel Hill)
526 and propagated and titrated using a plaque assay in Vero cells, which were cultured in Dulbecco's
527 Modified Eagle Medium (DMEM) supplemented with 5% fetal bovine serum (FBS). CVB3 (H3
528 strain) (Hardy et al., 2004) were propagated and titrated in HeLa cells cultured in Modified Eagle'
529 s Medium (MEM) supplemented with 5% FBS. For titration, serial dilutions of virus were added to
530 Vero (HSV-2) or CVB3 (HeLa) cell monolayers and incubated for 1 day at room temperature.
531 Following binding, cells were overlaid with a mixture of phenol red-free MEM and 0.5% agarose
532 and incubated for 48-72hrs at 37°C and 5% CO_2. The overlay was removed after incubation and
533 plaques were subsequently visualized by staining with crystal violet. Sendai virus (Cantell Strain)
534 was purchased from Charles River (PI-1, SV).
535

536 **HSV-2 infections**

537 8–10-week-old virgin female mice were used for all experiments. For HSV-2 infections females
538 were treated with 2mg of MPA (MedroxyProgesterone Acetate, NDC 66993-270-83) by
539 subcutaneous injection 5 days prior to infection to synchronize females in diestrus. Diestrus was
540 confirmed by vaginal cytology as previously described(Byers et al., 2012) 100 or 10,000 PFU of
541 HSV-2 was given by vaginal inoculation in a 10uL volume. HSV-2 was diluted in sterile PBS. Mice

542 were weighed and scored for pathology daily according to the following criteria: 0 no inflammation;
543 1 vaginal edema and redness; 2 hair loss or ulceration localized to the vaginal-anal area; 3 severe
544 ulceration, extensive hair loss extending beyond the vaginal-anal area; 4 overt disease signs; 5
545 paralysis; 6 death. Vaginal washes were taken by pipetting 110uL of PBS in and out of the vagina
546 5 times. Vaginal lavages were titrated by plaque assay on Vero cells as described above.
547

548 **CVB-H3 infections**

549 All CVB-H3 infections were performed in 8–10-week-old male mice. Mice were infected by oral
550 gavage with 1x10^8 pfu in 100uL of PBS. For viral burden experiments mice were sacrificed after
551 4 days, tissues were harvested and homogenized in DMEM using an Omni International Bead
552 Ruptor Elite (19-042E) at 4m/s for 1 minute using 2.8mm ceramic beads in 2 ml tubes (Omni
553 International 19-628). Viral burdens were quantified using a $TCID_{50}$ assay on HeLa cells. Serial
554 ten-fold dilutions of virus samples were prepared in complete medium and added to confluent
555 monolayers of HeLa 7B cells in 96-well plates. Cells were incubated for 3 days (37°C, 5% CO_2).
556 Cells were fixed and stained with crystal violet to visualize cytopathic effect (CPE). The dilution at
557 which 50% of wells showed CPE was recorded as the $TCID_{50}$ endpoint, using the Reed-Muench
558 method to calculate the viral titer.
559

560 **Generation of uterine single-cell suspension for scRNASeq**

561 Naturally cycling WT and Ifnε mice in estrus were confirmed by vaginal cytology (Byers et al.,
562 2012). The whole uterus was dissected and placed in 1x DPBS on ice until all tissues were
563 harvested. Uteruses were minced into 1-2mm pieces with dissecting scissors and placed into
564 2.5mL of D-PBS supplemented with Ca and Mg (Gibco, 14040117). Once all tissues were minced,
565 2.5 mLs of pre-warmed 2x disassociation media was added. 2x disassociation media was made
566 by dissolving 4mg/mL of Collegnase A (Roche, 10103578001) and 2U/mL of DNAase I (Roche
567 04536282001) in dispase (Corning 354235). Samples were incubated for 30 minutes at 37

568 degrees and were shaken vigorously for 30 seconds every 5 minutes. After incubation, enzymes
569 were inactivated by adding 0.5mL of FBS and samples placed on ice. Samples were pushed
570 through 100um filter (VWR 732-2759) using a plunger of a 1mL syringe. Cells were pelleted at
571 400g for 3 minutes at 4C and resuspended in 1mL of ice-cold PBS. 2ml of RBC lysis buffer
572 (Invitrogen, 00-4333-57) was added for 1 minute with a single inversion to mix, and then 10mLs
573 of 1% FBS-DPBS was added to each sample. Cells were pelleted at 400g for 3 minutes at 4C
574 and resuspended in 500uL of ice cold 1% FBS-PBS. Cells were counted and resuspended at a
575 final volume of $1.5x10^6$ cells/mL in 1% FBS-DPBS. Cells were kept on ice immediately dropped
576 off for scRNAseq processing.
577
578 **Generation of intestinal single-cell suspension for scRNASeq**
579 The entire length of the small intestine was dissected from age-matched, 8 week old WT and Ifnε
580 male mice and processed into a single cell suspension as previously described
581 (https://pubmed.ncbi.nlm.nih.gov/36880999/). Briefly, intestinal contents were flushed with 1X
582 HBSS (Sigma H4641), opened longitudinally, and minced into 1mL pieces and then washed twice
583 with 1X HBSS. Tissues were digested for 20 minutes in digestion media: 1X HBSS, 5%FBS
584 (Gibco A56707-01), 5mM EDTA (RPI E14000-250), 1mM DTT (Sigma D0632). Samples were
585 shaken vigorously to help release epithelial cells, and then the supernatant containing
586 epithelial cells was passed through a 100um cell strainer after allowing the residual tissue
587 segments to settle to the bottom of the tube. Samples were spun down at 2000RPM for 5
588 minutes, resuspended in 1mL of room temperature PBS, and then 2mL of RBC lysis buffer
589 (Invitrogen, 00-4333-57) was added and mixed into the sample by inverting. RBC lysis was
590 performed for 1 minutes at room temperature. 10mL of ice-cold 5%FBS-HBSS was added to
591 each sample, and then samples were strained through a 40uM filter. Cells were counted and

592 resuspended at a final volume of $1.5x10^6$ cells/mL in 5% FBS-HBSS. Cells were kept on ice
593 immediately dropped off for scRNAseq processing.
594
595 **Enteroid Growth and Single Cell Preparation**
596 Human fetal enteroid culture and differentiation were based on published protocols for adult stem
597 cells (Beumer et al., 2022; He et al., 2022; Pleguezuelos-Manzano et al., 2020). For expansion,
598 enteroids were passaged by single-cell dissociation in TrypLE (Gibco) at 37ºC for 5 min,
599 resuspended in 40 µl Matrigel (Corning) domes, and overlayed with expansion medium (ExM) for
600 7 days. For differentiation, enteroids were mechanically disrupted in DPBS, resuspended in 40 µl
601 Matrigel domes, grown in patterning medium (PaM) for 16 days and in differentiation medium
602 (DiM) for 3 days. For single-cell analysis, enteroids were expanded (Exp) or differentiated (Dif),
603 scraped into cold DPBS, pelleted 5 min at 400 xg, resuspended in TrypLE, and incubated at 37ºC
604 for 15 min. Enteroids were mechanically dissociated by pipetting up and down 30 times, diluted
605 in basal media, pelleted 5 min at 400 xg, resuspended in DPBS with 1% BSA, and filtered through
606 a 30 µm strainer. Basal media contained: 10 mM HEPES, 2 mM L-glutamine, and 100 U/ml
607 penicillin-streptomycin in Advanced DMEM/F12 (Gibco). Expansion media (ExM) additionally
608 contained: 1X B27 (Invitrogen), 1 mM N-acetylcysteine (Sigma), 50 ng/ml mouse EGF
609 (Peprotech), 100 ng/ml mouse Wnt3a, 500 ng/ml mouse R-Spondin, 100 ng/ml human noggin
610 (R&D Systems), 1x N2 (Invitrogen), 10 mM Nicotinamide (Sigma), 100 ng/ml human IGF-1, 50
611 ng/ml human FGF-2 (Peprotech), 500 nM A83-01 (Tocris), 10 nM PGE2 (R&D Systems), and 10
612 nM [leu15]-Gastrin I (Millipore). Patterning media (PaM) additionally contained: 1X B27, 1 mM N-
613 acetylcysteine (NAC), 50 ng/ml mouse EGF, 100 ng/ml mouse Wnt3a, 500 ng/ml mouse R-
614 Spondin, 100 ng/ml human noggin, 500 nM A83-01, and 2 ng/ml IL-22 (Peprotech). Differentiation
615 media (DiM) additionally contained 1X B27, 1 mM N-acetylcysteine (NAC), 50 ng/ml mouse EGF,
616 50 ng/ml BMP-2 and 50 ng/ml BMP-4 (Peprotech).
617

618 **Single-Cell RNA-seq Library Preparation and Data Analysis**

619 Publicly available datasets from cycling mouse tissue (Winkler et al., 2024) were downloaded
620 from ArrayExpress (E-MTAB-11491 and from human intestine were downloaded from GEO
621 (accession numbers: GSE185224, GSE171620, GSE125970) (Burclaff et al., 2022; Triana et al.,
622 2021; Wang et al., 2020). Fastq files from all novel single cell RNA sequencing were uploaded to
623 SRA under the bioproject ID PRJNA1329228.

624 For uterus tissue from WT and *Ifnε*$^{-/-}$ mice, single-cell RNA-seq libraries were prepared
625 from ~10,000 cells/mouse using the 10x Genomics Chromium Single Cell 3' Reagent Kit (v2
626 chemistry, Manual Part #CG00052) following the manufacturer's protocol. Briefly, single-cell
627 suspensions were loaded into the 10x Chromium Controller to capture and barcode individual
628 cells. Libraries were constructed, and sequencing was performed on an Illumina NovaSeq 6000
629 system (Illumina, San Diego) using an S2 flow cell, providing an average sequencing depth of
630 ~61,000 reads per cell. After sequencing, raw base call (BCL) files were processed with the 10x
631 CellRanger pipeline (v6.1.2, 10x Genomics) for demultiplexing, alignment to the mouse reference
632 genome (GRCm38), and quantification of gene expression. Quality control and post-processing
633 were carried out using the CellRanger count and aggregate functions to generate gene
634 expression matrices. Data analysis was performed using the Seurat package (Hafemeister and
635 Satija, 2019; Satija et al., 2015) (v4.0) in R. Cells were filtered to include those with at least 700
636 but no more than 12,000 unique expressed genes. Additionally, cells with over 10% mitochondrial
637 gene content were excluded from further analysis. To correct for batch effects, datasets from
638 individual animals were normalized using the SCTransform() function (v2) in Seurat, and
639 integration was performed using the FindIntegrationAnchors() and IntegrateData() functions.
640 Dimensionality reduction was conducted via principal component analysis (PCA) using the
641 RunPCA() function. Cell clusters were identified using Louvain clustering with the FindClusters()
642 function in Seurat. The optimal clustering resolution was determined by evaluating clustering
643 stability across a range of resolutions (0.2 to 1.0) using the clustree() package, with a resolution

644 of 0.3 selected for downstream analysis. For combined analyses of wild-type (WT) and *Ifnε*$^{-/-}$
645 datasets, previously integrated datasets were merged and further integrated using the Harmony
646 algorithm (Korsunsky et al., 2019) (v1.0) for batch correction and alignment. Differential
647 expression analysis between clusters was performed using the Wilcoxson rank sum test
648 implemented in Seurat's FindAllMarkers() function. Genes with a log2 fold change > 0.25 and an
649 FDR-adjusted p-value < 0.05 were considered significantly differentially expressed. Marker genes
650 for each cluster were identified by searching for positively enriched genes using the
651 aforementioned criteria.

652 Human fetal enteroid single-cell RNA-seq libraries were similarly prepared, sequenced
653 and analyzed with minor differences. ~10,000 cells/sample were targeted, providing an average
654 sequencing depth of ~61,000 reads per cell. After sequencing, BCL files were processed with the
655 10x CellRanger pipeline (v7.0.1, 10x Genomics) for demultiplexing, alignment to the human
656 reference genome (GRCh38), and quantification of gene expression. Cells were filtered to include
657 those with at least 3,000 but no more than 10,000 unique expressed genes. Cells with less than
658 2% or more than 20% mitochondrial gene content were excluded from further analysis. Individual
659 samples were merged and integrated using the FindIntegrationAnchors() and IntegrateData()
660 function into Exp and Dif. Percent mitochondrial genes, feature count, read count, and the
661 difference of G2M and S phase scores were regressed. For combined analysis, Exp and Dif were
662 merged and further integrated using the Harmony algorithm (Korsunsky et al., 2019) (v1.0) for
663 batch correction and alignment.

664 For intestine tissue from WT and *Ifnε*$^{-/-}$ mice, libraries were prepared targeting 20,000
665 cells/mouse using 10x Genomics v4 GEM-x 3' chemistry. Libraries were sequenced on a
666 NovaSeq X plus using 2 lanes of a 25B flow cell. Data was analyzed similarly to the uterine
667 tissue, but with some key differences. Data was analyzed using Seurat version 5.3.0 (Hao et al.,
668 2024). Cells were filtered to include those with at least 1,000 but no more than 12,000 unique
669 genes. Cells with greater than 15% mitochondrial gene counts were excluded from further

670 analysis. Individual samples were merged into a split object and normalized and scaled using
671 NormalizeData() and ScaleData() with *Ifne* explicitly retained as a variable feature. WT and Ifn*ε*
672 samples were integrated separately using Harmony Integration and the IntegrateLayers()
673 function. Unique clusters were identified using a resolution of 0.6. To improve detection of lowly
674 expressed transcripts, we applied the ALRA (Adaptively-thresholded Low Rank Approximation)
675 algorithm (Linderman et al., 2022). Differentially expressed genes between WT and *Ifnε*$^{-/-}$
676 clusters were determined using DESeq2.
677
678 **Primary cells**
679 Primary human cells were purchased from Lifeline Cell Technologies (FC-0078, FC-0083) and
680 thawed into 24-well or 6-well plates according to manufacturer instructions. At 90% confluency
681 cells were treated with PAMPS or infected at the following concentrations; polyIC float (Invivogen,
682 tlrl-picw) 10ug/mL; polyIC transfection (Inviogen, tlrl-picw) 1ug/mL (0.5ug/well); cGAMP
683 transfection (Invivogen, tlrl-nacga23-02) 10ug/mL; SeV Cantell 20HAU well; HSV-2 333 MOI of
684 1; LPS float (invivogen, tlrl-eklps) 100ng/mL. cGAMP and polyIC transfected using
685 xTREMEgene9 (Roche, XTG9-RO) according to manufacturer's instructions.
686
687 **qPCR and bulk RNA Sequencing**
688 RNA was extracted from cells using Qiagen Rneasy mini kit (74104) according to
689 manufacter instructions. *IFNε*, *IFNβ*, and *ACTB* RNA levels were detected by qRT-PCR using IDT
690 PrimeTime Std qPCR Assay Primer Probes: *IFNε* Hs.PT.58.4812867; *IFNβ1*
691 Hs.PT.58.39481063.g, ACTB: Hs.PT.39a.22214847 and Itaq one step kit (BIO-RAD 172-5140).
692 qRT-PCR was run using a Biorad Opus. For bulk RNA sequencing, libraries were prepared by the
693 Duke Center for Computational Biology and Genomics (GCB) using a mRNA standed KAPA
694 hyperprep kit. Sequencing was performed an Illumina Novaseq X Plus using 100bp paired end
695 sequencing and targeting 10 billion reads across all samples. Reads were aligned to the human

696 genome using Qiagen CLC Genomics (v20). Differential expression analysis was performed using
697 DESeq2. Briefly, raw count data were imported into R and DESeq2 (Love et al., 2014) was used
698 to normalize counts and identify differentially expressed genes between specified conditions.
699 Genes with an adjusted p-value < 0.05 and log2 ± 2 fold change were considered significantly
700 differentially expressed. Fastq files were uploaded to SRA under the bioproject ID
701 PRJNA1329228.
702
703 **ELISA**
704 IFNε and IFNβ protein levels were detected by ELISA (R&D Systems, DY9667-05, DY814-05).
705 IFNε and IFNβ levels were normalized to total protein quantified by Pierce BCA Assay (23227).
706 Cellular lysates were generated using M-PER Mammalian Protein extraction reagent (Thermo
707 Scientific 78501).
708
709 **16S Ribosomal Sequencing**
710 Fecal samples were collected from adult *Ifnε*$^{+/-}$ *and Ifnε*$^{-/-}$ littermates and sent to Microbiome
711 Insights for 16S sequencing and analysis. Specimens were placed into a MoBio PowerMag Soil
712 DNA Isolation Bead Plate. DNA was extracted following MoBio's instructions on a KingFisher
713 robot. Bacterial 16S rRNA genes were PCR-amplified with dual-barcoded primers targeting the
714 V4 region (515F 5'-GTGCCAGCMGCCGCGGTAA-3', and 806R 5'-
715 GGACTACHVGGGTWTCTAAT-3'), as previously described (Kozich et al., 2013). Amplicons were
716 sequenced with an Illumina MiSeq using the 300-bp paired-end kit (v.3). Sequences were
717 denoised, taxonomically classified using Silva (v. 138) as the reference database, and clustered
718 into 97%-similarity operational taxonomic units (OTUs) with the mothur software package (v.
719 1.44.1) (Schloss et al., 2009), following the recommended procedure
720 (https://www.mothur.org/wiki/MiSeq_SOP; accessed Nov 2020). Alpha diversity was estimated
721 with the Shannon index on raw OTU abundance tables after filtering out contaminants. The

722 significance of diversity differences was tested with ANOVA or linear mixed model depending on
723 the study design. To estimate beta diversity across samples, we excluded OTUs occurring with a
724 count of less than 3 in at least 5 % of the samples and then computed Bray-Curtis indices. We
725 visualized beta diversity, emphasizing differences across samples, using Principal Coordinate
726 Analysis (PCoA) ordination. Variation in community structure was assessed with permutational
727 multivariate analyses of variance (PERMANOVA) with treatment group as the main fixed factor
728 and using 999 permutations for significance testing.A dot-dash circle in ordination plot represent
729 for the central of each cluster (Nguyen et al., 2020). All analyses were conducted in the R
730 environment.
731

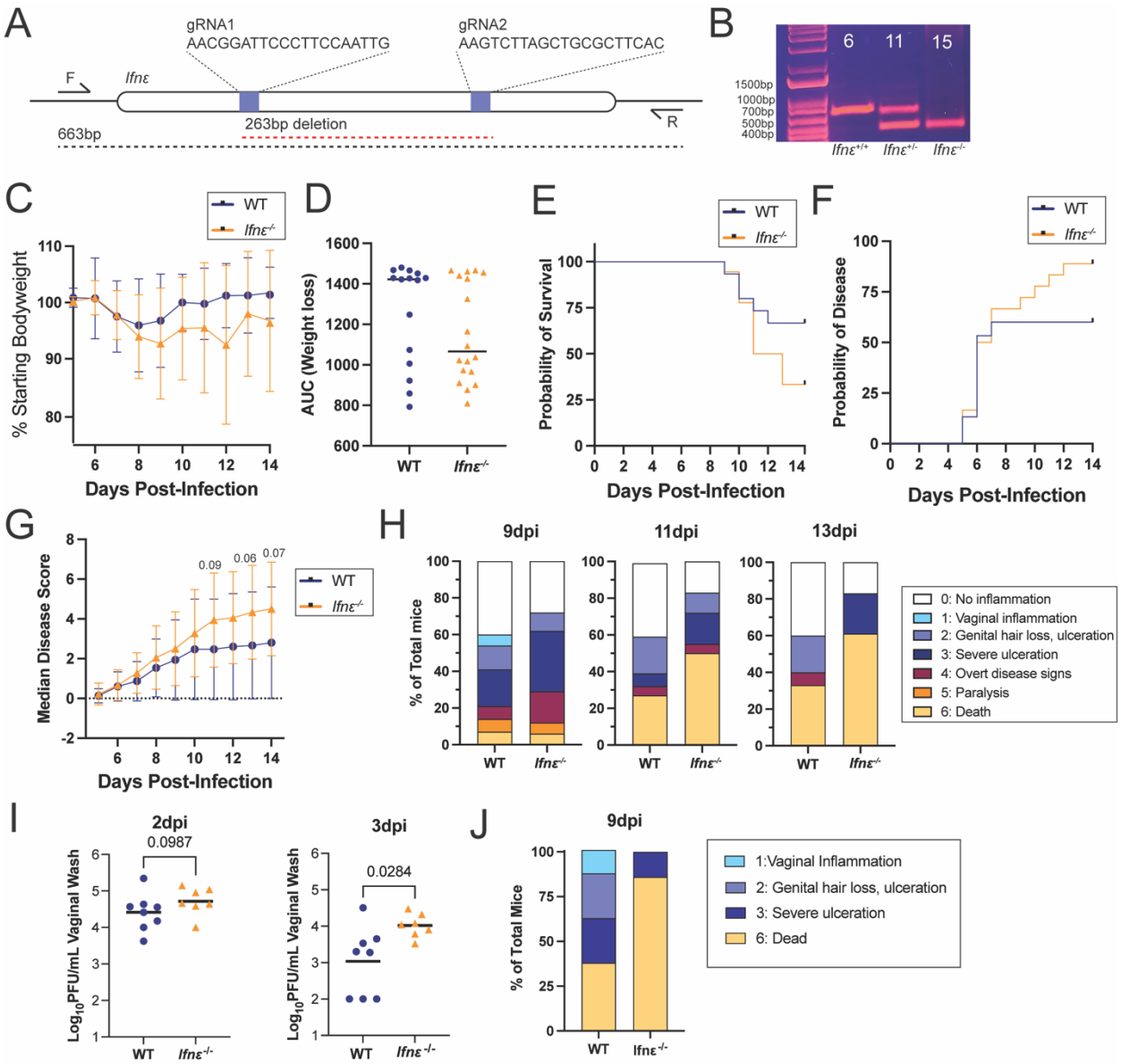

Figure 1: Increased HSV-2 Susceptibility in *Ifnε* Deficient Mice Generated via iGONAD CRISPR/Cas9. A) Schematic of CRISPR/Cas9 knockout strategy. **B)** Representative PCR genotyping results from the first generation of pups born to dams that underwent iGONAD gene editing. Mouse 6 (*Ifnε*$^{+/+}$), 11 (*Ifnε*$^{+/-}$) and 15 (*Ifnε*$^{-/-}$) are shown. Mouse 15 was chosen as the founding sire for the line. **C-H)** WT (n=15) and *Ifnε*$^{-/-}$ (n=18) females were infected with 100PFU of HSV-2 333 and weighed and monitored for disease signs daily. Weight loss (C,D), survival (E), and disease onset (F) are shown. Disease onset (F) includes any observable pathology score. Median clinical score is shown in G, and in (H), frequencies of clinical scores are shown

741 at multiple days post-infection (dpi) from 9-13dpi. Key at right. Differences in median clinical
742 score was determined by Mann-Whitney test in Graphpad Prism. **I-J).** WT (n=8) and *Ifnε*$^{-/-}$ (n=7)
743 females were infected with 10,000PFU of HSV-2 333. Vaginal lavages were collected at 2 and
744 3dpi and titrated by plaque assay. Significant differences were calculated by T-test in Graphpad
745 Prism. Individual animals are depicted by symbols in (I). Frequencies of clinical scores are
746 shown at 9dpi in (J).
747
748
749
750
751
752

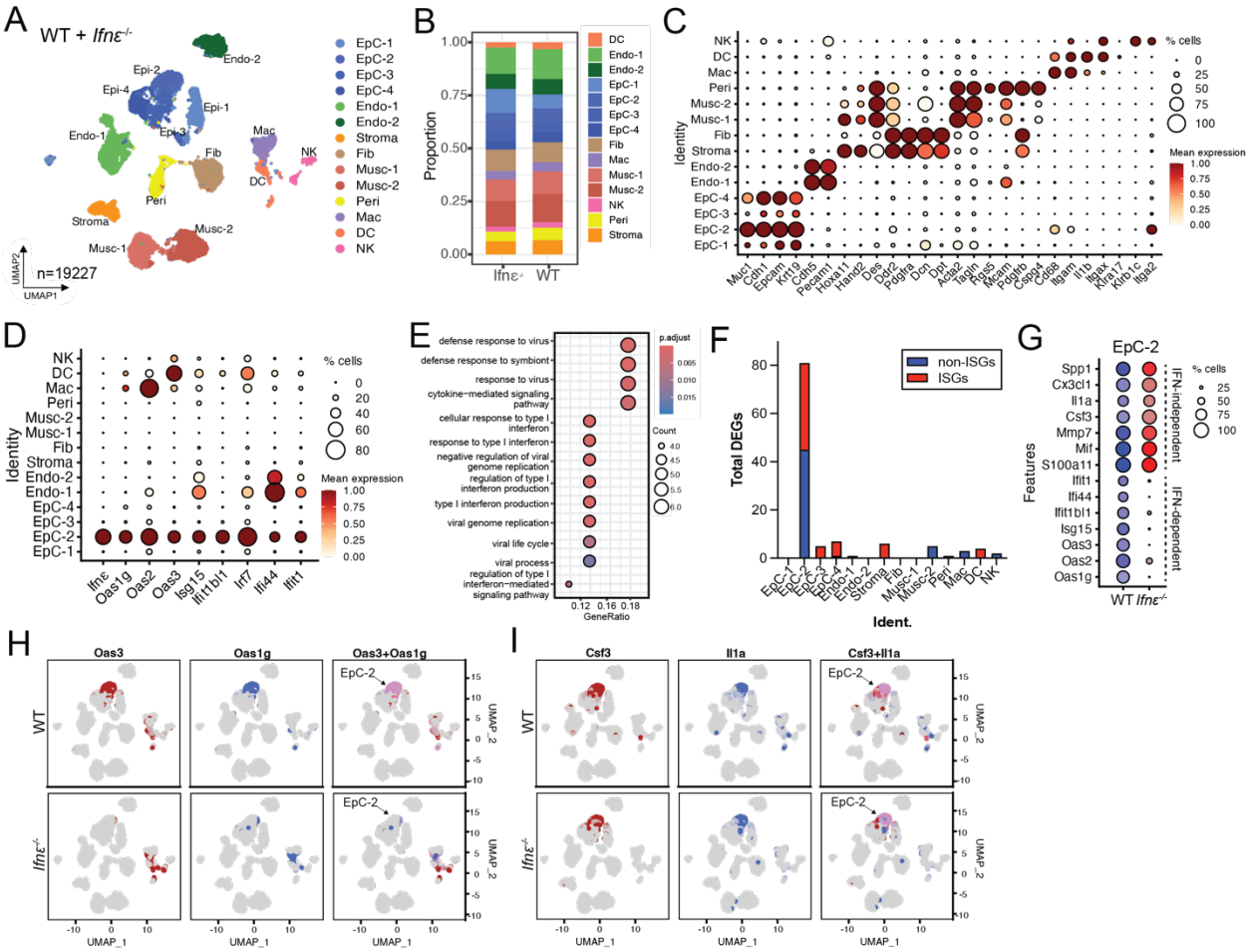

Figure 2. *Ifnε*$^{-/-}$ Mice Lack Basal ISG Expression in Uterine Epithelial Cells. A) UMAPs showing uterine cell clusters from *Ifnε-/-* and WT mice. **B)** Bar plot of the proportions of each cell cluster in *Ifnε-/-* and WT mice. **C)** DotPlot of canonical cell type markers in each cell cluster. Key and scale at right. **D)** DotPlot of *Ifnε* and ISG expression in each cell cluster. Key and scale at right. **E)** Pathway analysis on differentially expressed genes in *Ifnε-/-* and WT uteruses. Shown are the gene counts per pathway and the p-value of each pathway. **F)** The total number of DEGS in each cluster. ISGs are shown in red and non-ISGs are shown in blue. **G)** DotPlot showing ISG and cytokine expression levels split by mouse genotype. Scale at right. **H)** FeaturePlots showing co-expression of *Oas3* and *Oas1g* in either WT (top) or *Ifnε*$^{-/-}$ (bottom) samples. **I)** FeaturePlots showing co-expression of *Csf3* and *Il1a* in either WT or *Ifnε*$^{-/-}$ samples.

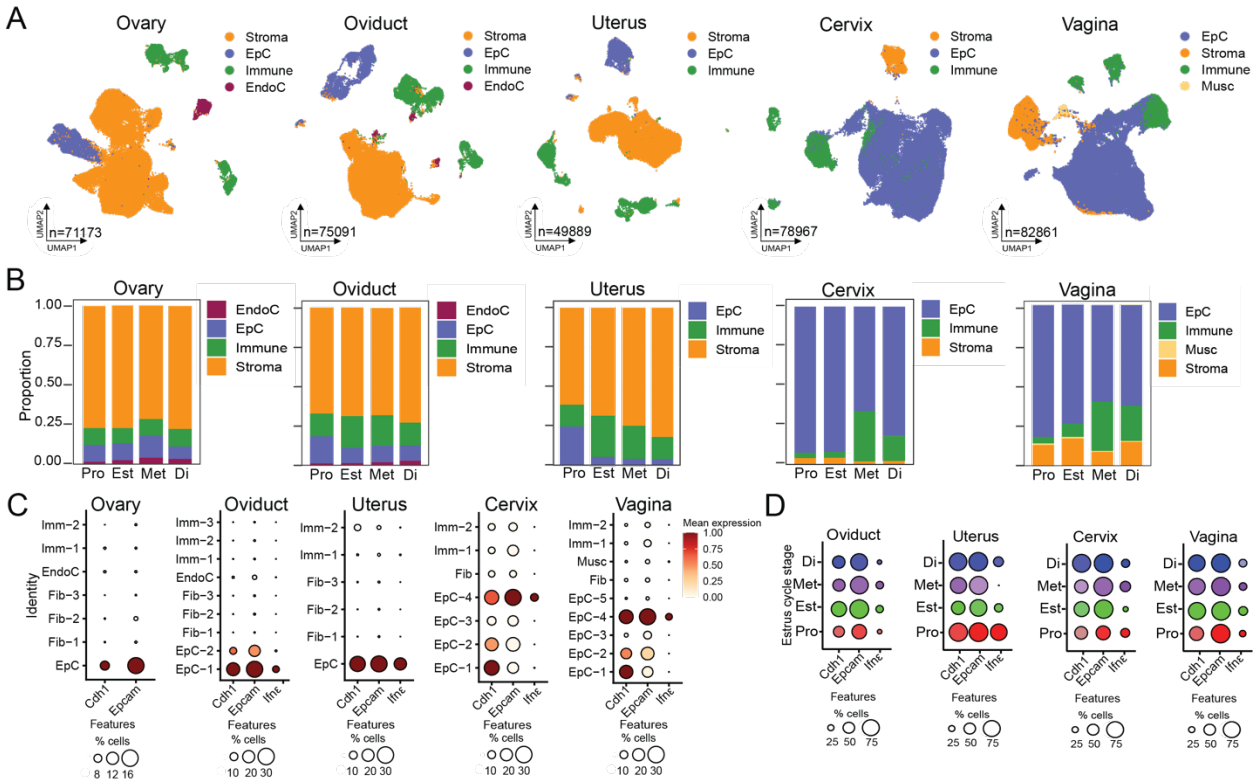

Figure 3: *Ifnε* is expressed in epithelial cells of the female reproductive tract throughout the estrous cycle. A) UMAPS showing clustering of stromal (Stroma, orange), epithelial (EpC, blue), immune (Immune, green), endothelial (EndoC, red), and muscular (Musc, yellow) cells within the different tissues of the female reproductive tract (FRT). **B)** The proportions of each cell type split by estrous stage: Proestrous (Pro); Estrous (Est); Metestrous (Met), and Diestrous (Di). **C-D)** DotPlots showing expression of epithelial cell markers and *Ifnε* in all clusters (C) or only in clusters that express *Ifnε* split by estrous stage (D).

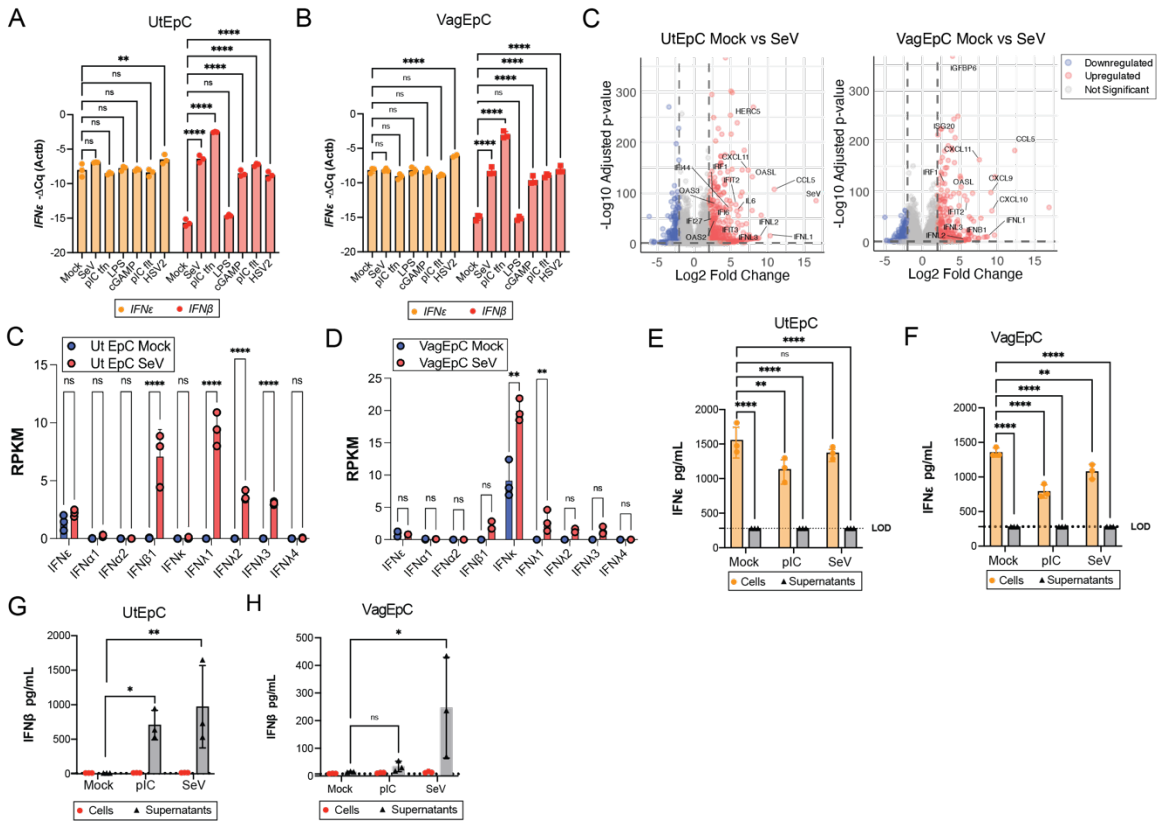

Figure 4: IFNε is retained intracellularly in primary human epithelial cells and is not induced by viral infections. **A, B),** Primary human uterine (UtEpV) (A) or vaginal (VagEpC) (B) epithelial cells were treated infected with Sendai virus cantell (SeV, 200HAU) or HSV2 (MOI of 1), treated with LPS or poly(I:C), or transfected with cGAMP or poly(I:C). Cells were harvested 20hpi and *IFNE* and *IFNB* levels were quantified by qRT-PCR. **C),** Volcano plots of differentially expressed genes ($\log_2 \geq 2$ or ≤ -2, $p_{adj} \leq 0.01$) in UtEpC (left) or VagEpC (right) infected for ~24hrs with 200HAU SeV. Upregulated genes are shown in red and downregulated genes are shown in blue. Select gene names are shown in black. **D, E),** Reads per kilobase of transcript, per million mapped reads (RPKM) of the indicated IFN gene in Mock- (blue) or SeV-infected (red) UtEpC (D) or VagEpC (E). **F-I),** IFNε(F, G) and IFN-β (H, I) protein levels were measured from cell lysates and cell supernatants from uterine (F, H) or vaginal (G, I) epithelial cells by ELISA . Significance

was determined by two-way ANOVA using a Tukey's test for multiple comparisons (*, $p<0.05$, **$p<0.01$, ***$p<0.001$, ****$p<0.0001$, ns ,not significant).

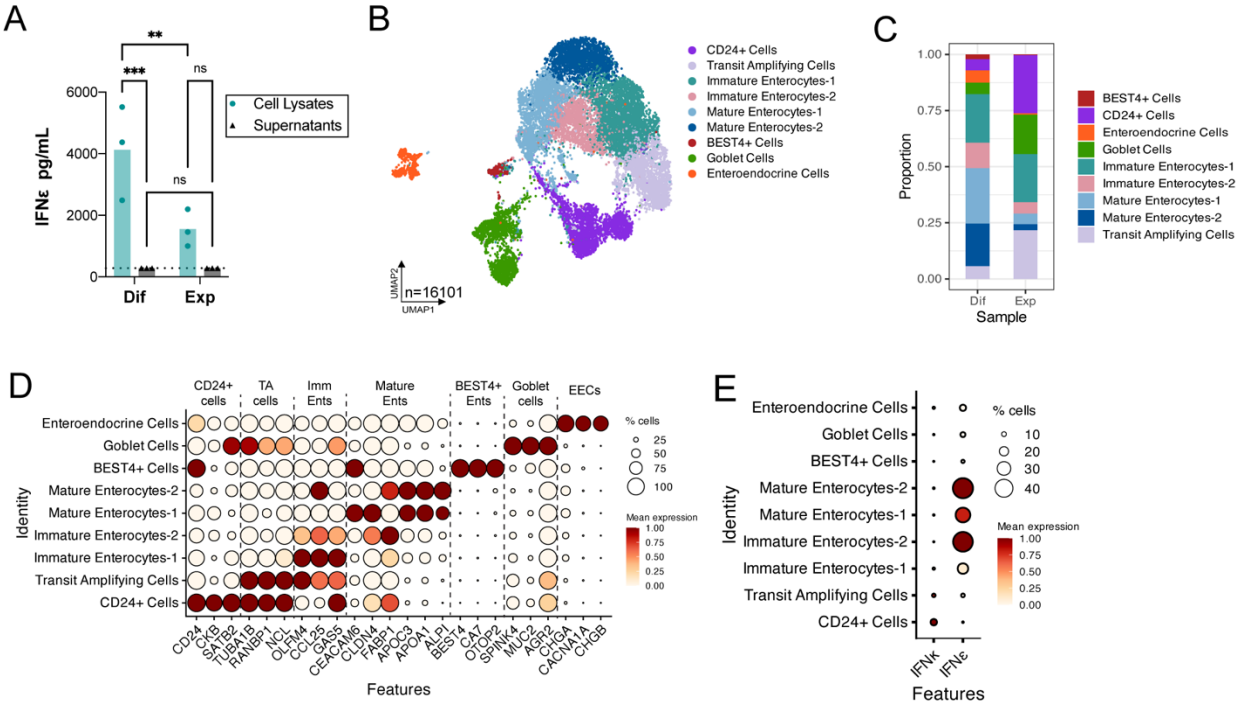

Figure 5: IFNε is expressed in human intestinal epithelial cells and is retained intracellularly. (A-E), Human enteroids were grown under expansion (Exp) or differentiating conditions (Dif) and then analyzed by scRNAseq. **A)** IFNε levels in supernatants and cell lysates from Exp and Dif enteroids, measured by ELISA. Data points represent IFNε concentration across experimental conditions, with significance determined by two-way ANOVA followed by multiple comparisons to assess differences between groups (ns, not significant, **p<0.01, ***p<0.001). **B)** UMAP plot depicting distinct cell clusters identified in the dataset. Each cluster is represented by a unique color, indicating cellular heterogeneity and grouping based on transcriptomic profiles. **C)** Bar plot depicting cell enrichment under Exp or Dif conditions. **D),** DotPlot of canonical cell makers used to define clusters. Key and scale at right. **E)** *IFNε* and *IFNκ* expression in cell clusters.

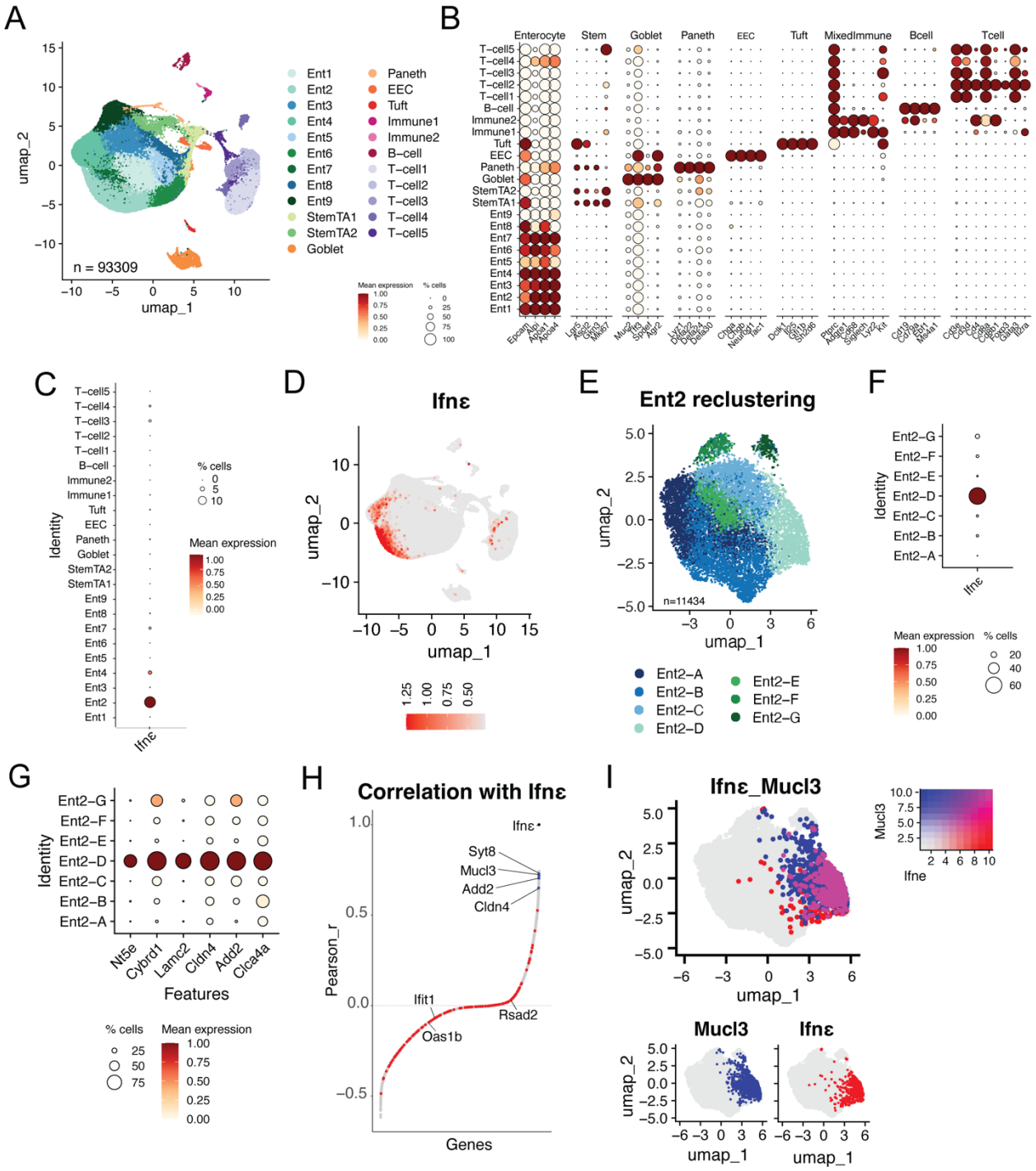

820

821 **Figure 6: *Ifnε* is expressed in villous-tip enterocytes of the mouse small intestine.** Single-

822 cell suspensions were generated from WT and *Ifnε*$^{-/-}$ mouse small intestines and analyzed by

823 scRNA-seq. **(A)** UMAP plot revealed distinct cell clusters, including enterocytes (Ent), stem or

transit-amplifying cells (Stem/TA), enteroendocrine cells (EEC), and immune cell populations expressing macrophage, dendritic cell, and mast cell markers. **(B)** Canonical marker genes used to define each cluster are shown in a dot plot. **(C, D)** *Ifnε* expression was detected primarily in enterocytes, as shown in both dot plots (C) and feature plots (D). **(E)** To further resolve enterocyte heterogeneity, cells within Ent2 were subsetted and reclustered, revealing distinct subclusters. **(F)** *Ifnε* expression across these subclusters is shown in a dot plot. (G) Dotplot showing expression of top markers in Ent2-D, the cluster that expresses *Ifnε* **(H)** Correlation analysis between *Ifnε* and all other genes expressed in Ent2 demonstrated no association with interferon-stimulated genes (ISGs, shown in red) but revealed strong correlations with villous tip–associated genes, including *Mucl3*. **(I)** A feature plot confirmed the overlap between *Ifnε* and *Mucl3* expression within Ent2, indicating that *Ifnε* is enriched in villous-tip enterocytes.

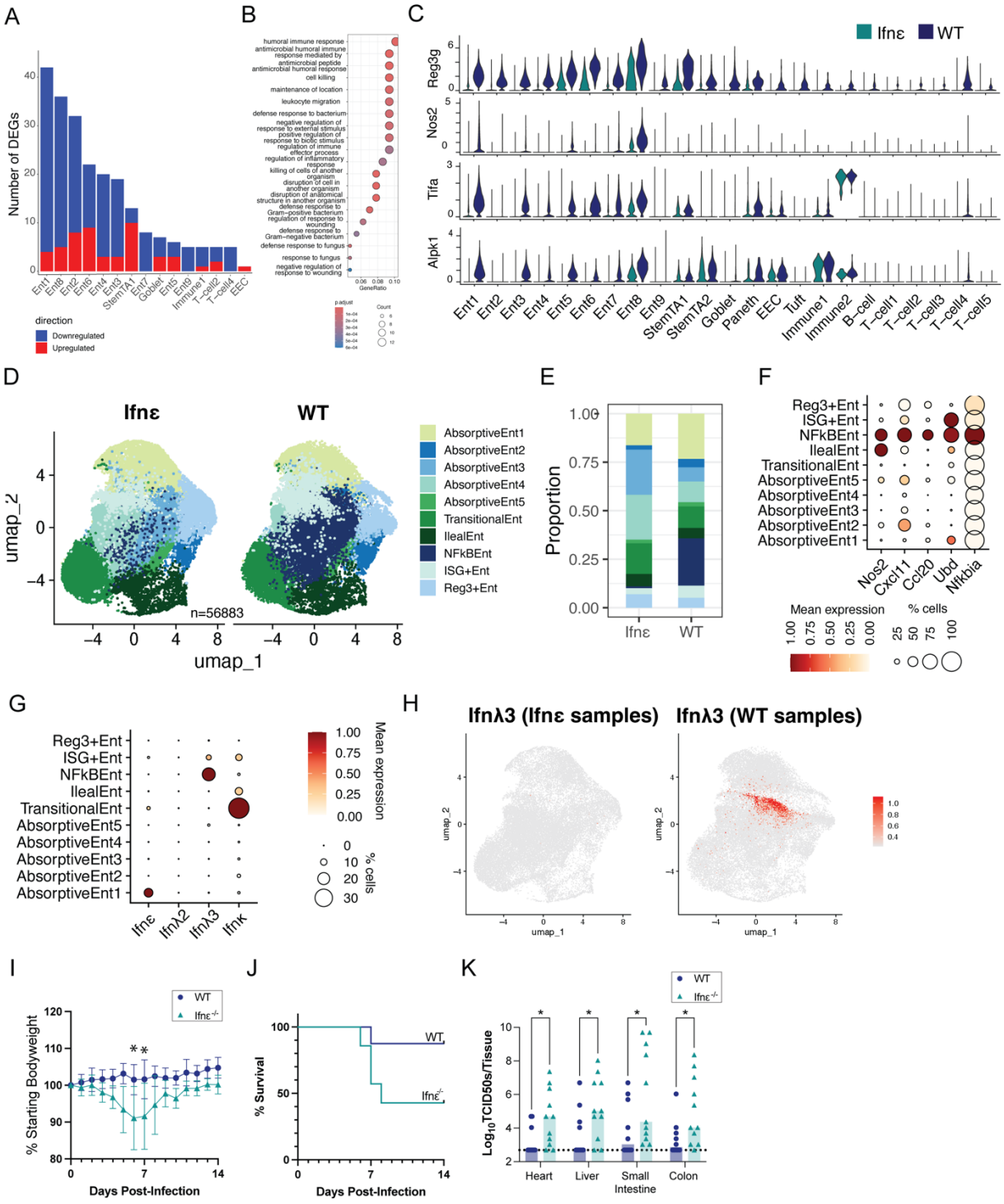

Figure 7: Loss of *Ifnε* Depletes Inflammatory Enterocyte Subsets and Increases Susceptibility to Enteric Viral Infection. A) Pseudo bulk analysis using DESEQ2 was performed for each cluster in the entire tissue intestinal single cell RNAseq data set introduced in

840 Fig. 6. Total number of DEGs (in *Ifnε*$^{-/-}$ samples compared to WT) are shown for each cluster.
841 Clusters not graphed (B-cell, Immune2, Paneth, STEMTA2, T-cell1, T-cell3, T-cell5, Tuft) had no
842 DEGs. **B)** GO analysis was performed on the list of total identified DEGs and pathways identified
843 were graphed. Scales and are below. **C)** Violin plots of gene expression of DEGs identified
844 inmultiple clusters split by WT (dark blue) and *Ifnε*$^{-/-}$ (teal) samples. **(D-H)** All cells within enterocyte
845 clusters 1-8 (Enterocyte cluster 9 was excluded as its top markers were all mitochondrial genes)
846 were subsetted from the original dataset and reanalyzed. **D)** Split UMAP depicting the clustering
847 of the Ent1-9 subcluster. **E)** Bar plot showing the proportion of cells in each cluster in either WT
848 or *Ifnε*$^{-/-}$ samples. **F)** Dot plot showing the expression of top markers of the NFkB Enterocyte
849 cluster. Key and scale below. **G)** Dot plot showing expression of all interferons detected in the
850 Ent1-9 subcluster. **H)** Feature plot showing expression of *Ifnλ3* in either *Ifnε*$^{-/-}$ (left) or WT (right)
851 samples. Scale to the right. **(I-K)** WT and *Ifnε*$^{-/-}$ mice were orally infected with $1x10^8$ PFU of CVB-
852 H3 and weighed and monitored daily for signs of illness (I,J), or sacrificed at 4 days post infection
853 (dpi). Viral burdens in tissues (K) were determined by TCID50. Significant differences in weight
854 (*$p<0.05$) were calculated by t-test in Graphpad Prism. Differences in viral burden were calculated
855 by Mann-Whitney test (*$p<0.05$).

856

857

858
859
860
861
862
863
864
865
866
867
868
869
870
871
872

873

A

```
Ifnε-/-   ATGGTTCACAGACAGCTCCCTGAAACGGTGTTGCTGCTCTTGGTTTCTTCCACTATCTTC
WT        ATGGTTCACAGACAGCTCCCTGAAACGGTGTTGCTGCTCTTGGTTTCTTCCACTATCTTC

Ifnε-/-   TCCCTAGAACCGAAACGG------------------------------------------
WT        TCCCTAGAACCGAAACGGAAACGGATTCCCTTCCAATTGTGGATGAACAGAGAAAGCCTA

Ifnε-/-    ------------------------------------------------------------
WT        CAACTACTGAAACCTTTGCCAAGCTCGTCAGTCCAGCAGTGTCTAGCACACAGGAAGAAT

Ifnε-/-   ------------------------------------------------------------
WT        TTCCTGCTTCCTCAGCAGCCTGTGAGTCCTCACCAGTACCAAGAGGGACAGGTGCTGGCT

Ifnε-/-   ------------------------------------------------------------
WT        GTTGTGCACGAGATCCTTCAGCAGATCTTCACGCTCCTCCAGACACATGGGACTATGGGC

Ifnε-/-   ---------------------------------------------CGGCAGCTGGAATAC
WT        ATTTGGGAGGAAAACCATATAGAAAAAGTCTTAGCTGCGCTTCACCGGCAGCTGGAATAC
```

874
875 **Supplemental Figure 1. (A)** Sequence alignment following Sanger sequencing of genomic DNA
876 isolated from an *Ifnε*$^{-/-}$ mouse (top) or wild-type (WT, bottom) mouse. Bold red sequences denote
877 location of gRNAs (gRNA1 and gRNA2). Dashes denote sequence missing in the *Ifnε*$^{-/-}$ mouse.
878
879
880
881
882
883

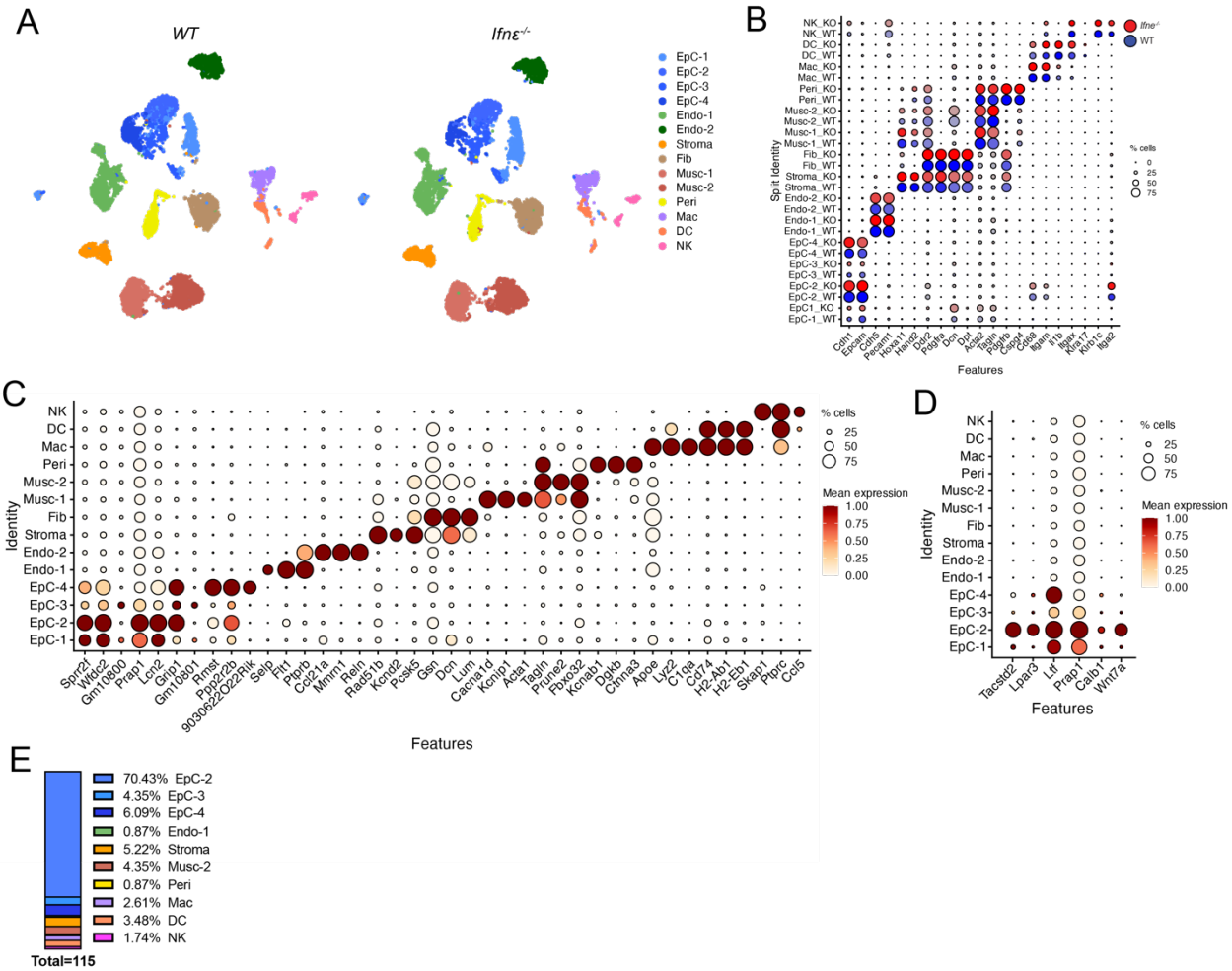

Supplemental Figure 2. (A), UMAP of cell clusters in uterine tissue isolated from WT (left) of Ifnε$^{-/-}$ mice (right) split by genotype. (B), DotPlot of canonical cell markers in WT (blue) or *Ifnε*$^{-/-}$ (red) mice. **(C),** DotPlort of cell type markers in the combined dataset from WT and *Ifnε*$^{-/-}$ mice. Scale and key at right. (D), DotPlot of luminal cell markers in WT and *Ifnε*$^{-/-}$ dataset. Key and scale at right. (E), Bar plot indicating the cell clusters associated with differentially upregulated genes (115 total) in WT mice compared to *Ifnε*$^{-/-}$ mice. The percent is shown at right.

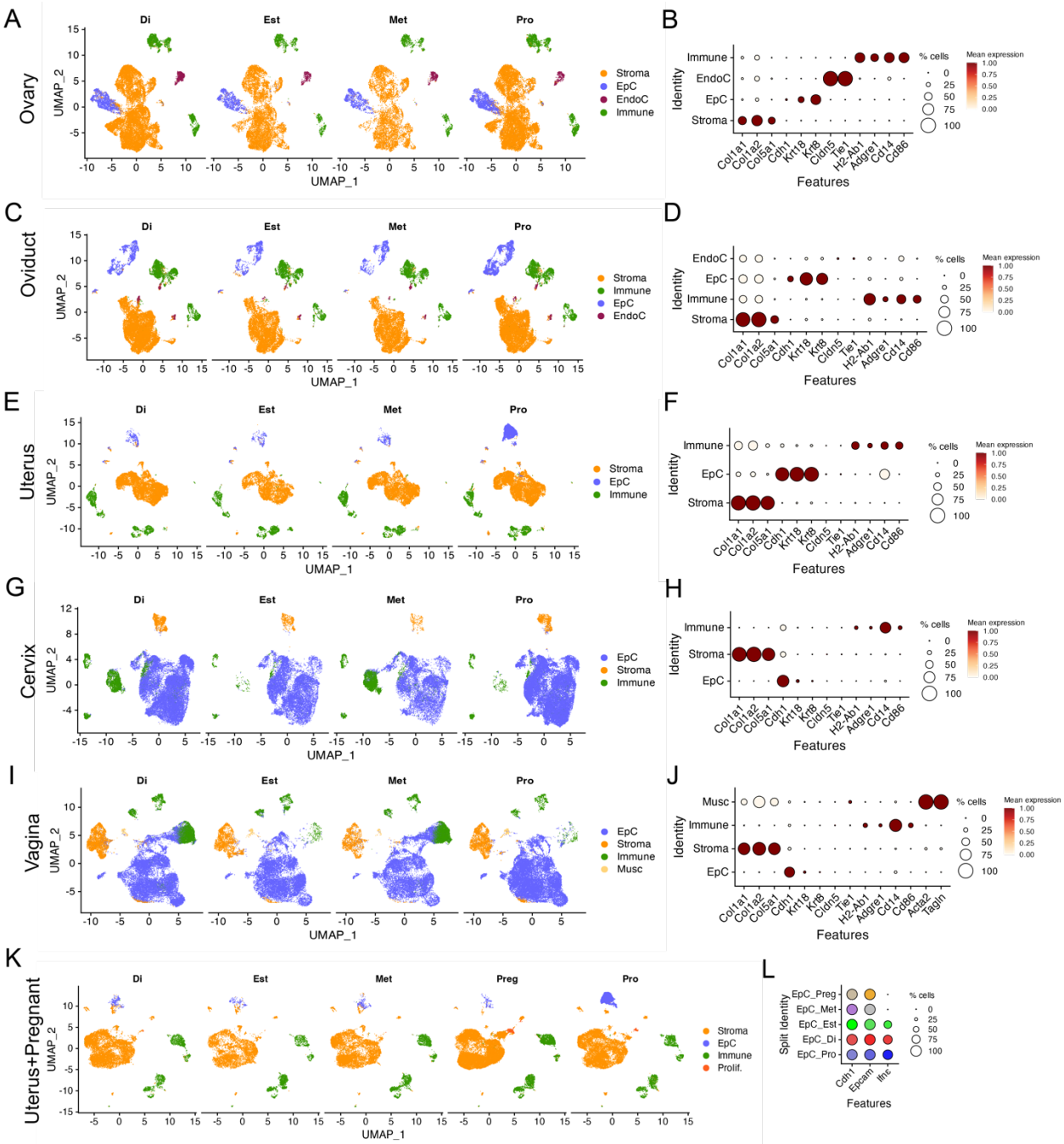

Supplemental Figure 3. (A, C, E, G, I) UMAPS showing clustering of stromal (Stroma, orange), epithelial (EpC, blue), immune (Immune, green), endothelial (EndoC, red), and muscular (Musc, yellow) cells within distinct phases of the estrous cycle the different tissues of the female reproductive tract (FRT) shown at left. **(D, F, H, J),** DotPlot of canonical markers in Oviduct (D), Uterus (F), Cervix (H), Vagina (J), and Uterus (J). **(K),** UMAP of uterine tissue throughout the estrous cycle and pregnant uterus (Preg). **(L),** DotPlot of cadherin-1 (*Cdh1*), *Epcam*, and *Ifnε* in uterine tissue split by phase of the estrous cycle or pregnancy (in orange).

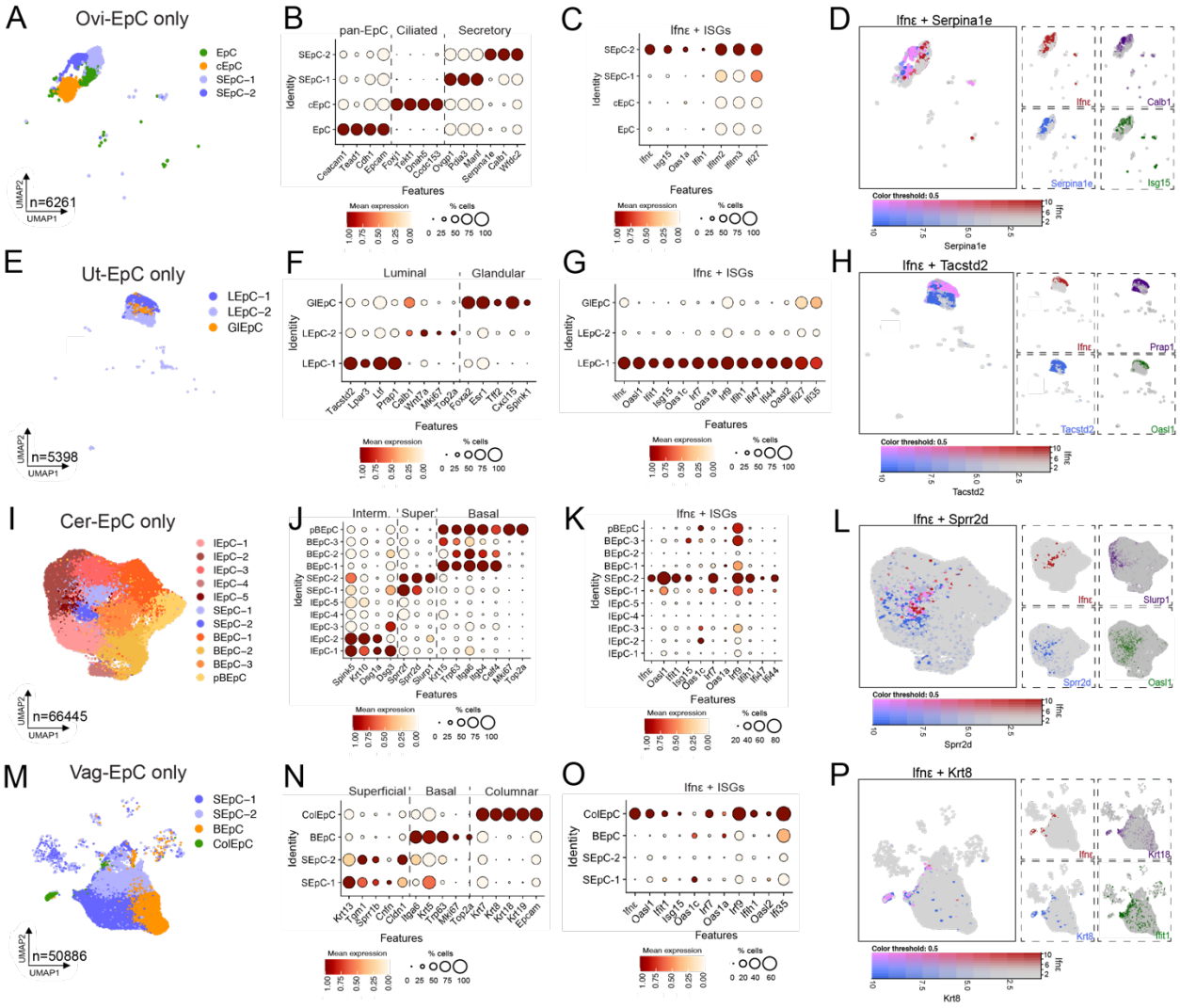

Supplemental Figure 4. Epithelial cell clusters from Figure 2 were reclustered. **A,E,I,M)** UMAPS showing clustering of epithelial cell types within each tissue. Oviduct **(A)**: general epithelial cells (Epc), ciliated epithelial cells (cEpC), and secretory epithelial cells (SEpC-2). Uterus **(E)**: luminal epithelial cells (LEpC) and glandular epithelial cells (GlEpC). Cervix **(I)**: intermediate epithelial cells (IEpC), superficial epithelial cells (SEpC), basal epithelial cells (BEpC), and parabasal epithelial cells (pBEpC). Vagina **(M)**: superficial epithelial cells (SEpC), basal epithelial cells (BEpC), and Columnar epithelial cells (ColEpC). **B,F,J,N).** Dot plots showing markers of each epithelial subpopulation. **C,G,K,O)** Dot plot showing Ifnε and ISG expression within each cluster. **D,H,L,P)** Feature plots showing expression and coexpression of Ifnε and a top marker for the cluster in which it is expressed.

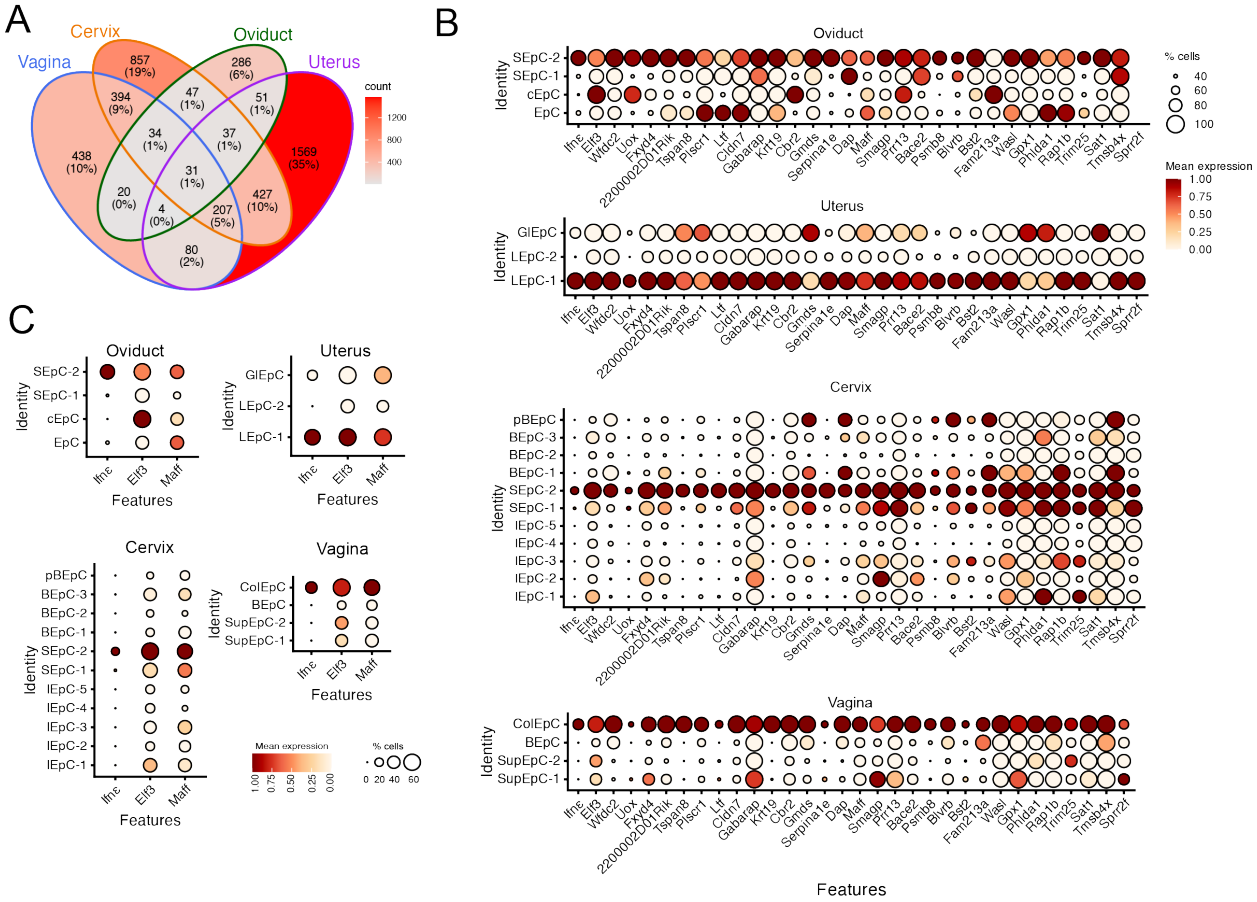

Supplemental Figure 5. (A), Venn diagram denoting the overlap of gene enriched in Ifnε-expressing clusters from Oviduct (green), Uterus (purple), Cervix (orange), and Vagina (blue). Key at right with red indicating the highest number of genes. The percent of overlap is also shown. **(B),** DotPlot of the genes differentially enriched in *Ifnε*-expressing clusters in Oviduct (top), Uterus (second from top), Cervix (second from bottom), and Vagina (bottom). Key and scale at right. **(C),** DotPlot of the expression of *Ifnε*, *Elf3*, and *Maff* in Oviduct, Uterus, Cervix, or Vagina as indicated. Key and scale at bottom.

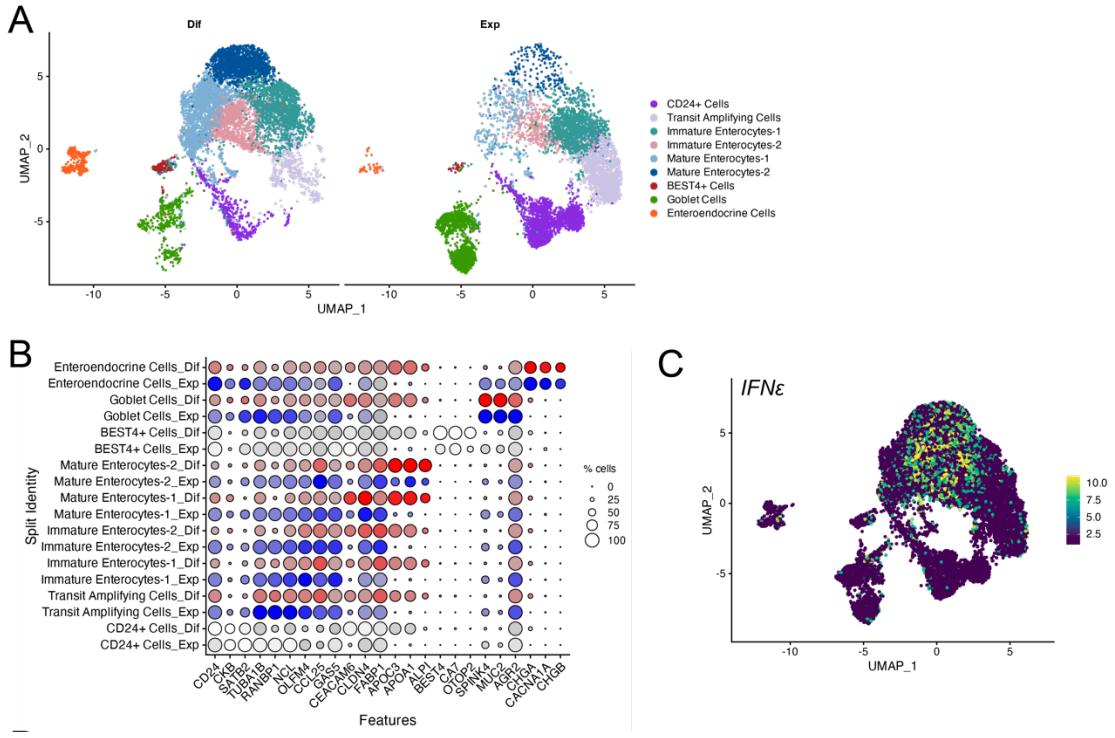

Supplemental Figure 6. (A), UMAP of cell clusters in enteroids cultured under expansion (Exp) or differentiated (Dif) conditions. **(B),** DotPlot of canonical makers in enteroids split by either Dif (red) or Exp (blue) growth conditions. **(C),** FeaturePlot of *IFNE* in enteroids. Scale at right.

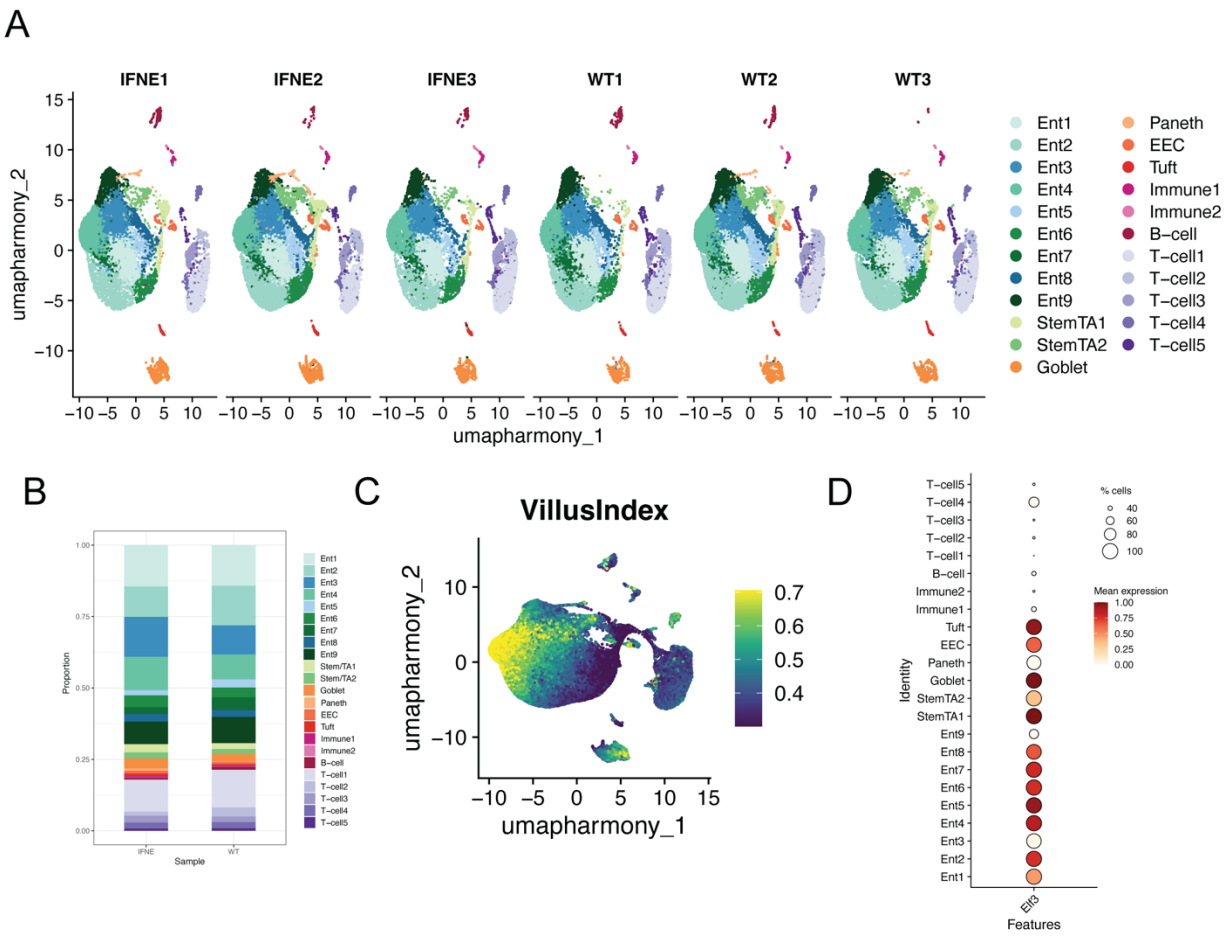

Supplemental Figure 7: (A), UMAP of cell clusters in intestinal tissue isolated from WT or Ifnε$^{-/-}$ mice (right) split by sample. **(B)** Bar plot showing the proportion of cells in each cluster split by WT or Ifnε$^{-/-}$ mice **(C)** Feature plot showing a villus index score for each cell as calculated as follows: (expression top genes/(expression top genes + expression bottom genes). 62 bottom landmark genes and 43 top landmark genes were included that were identified in Moor et al. 2018. **(D)** Dotplot showing proportion and expression levels of *Elf3* in each cluster. Scale and key to the right.

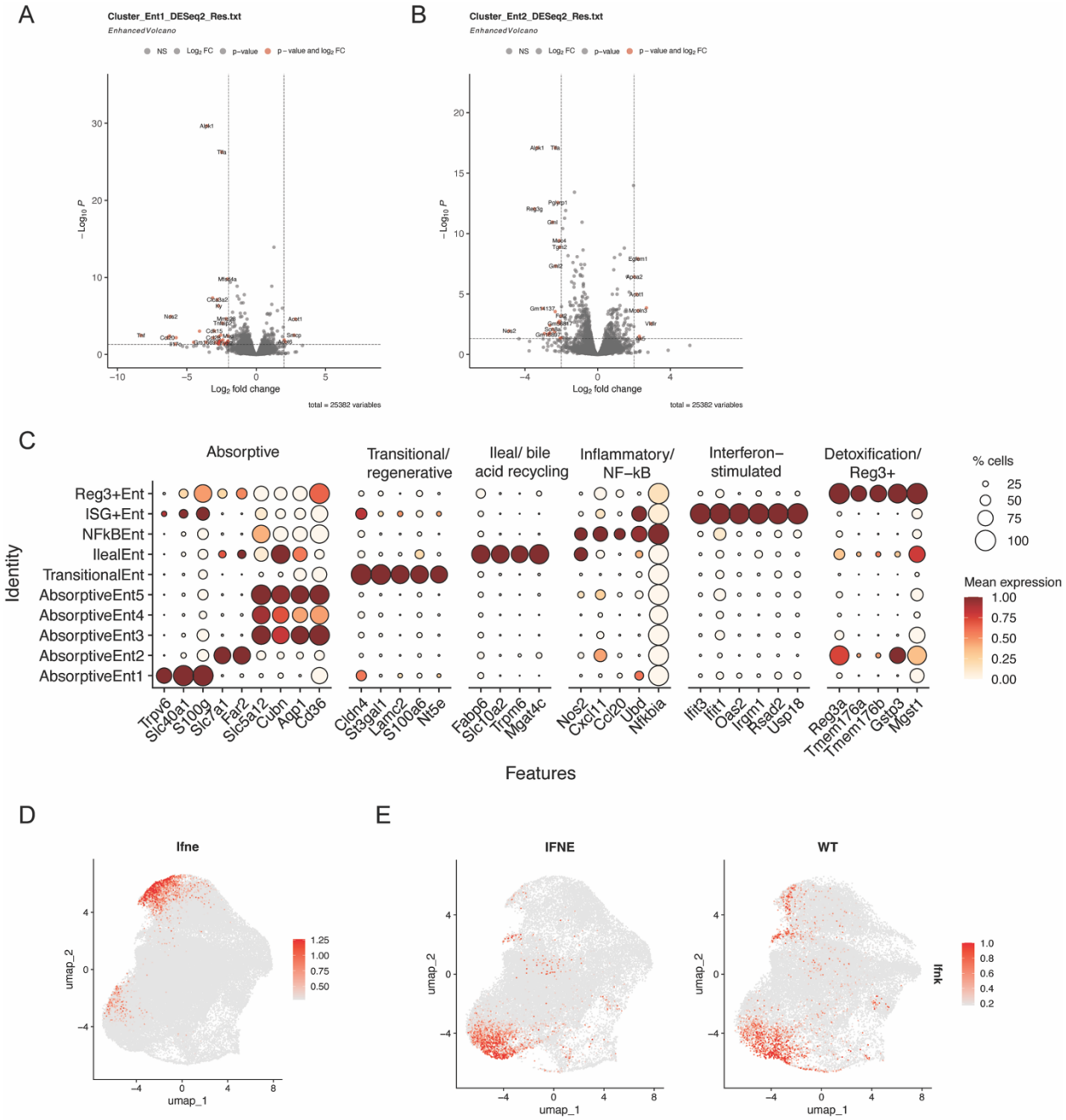

Supplemental Figure 8: (A-B) Volcano plots showing genes differentially expressed in Ifnε$^{-/-}$ samples compared to WT in clusters Ent1 (A) and Ent2 (B). DEGs were calculated by DESeq2. **(C).** DotPlot showing markers used to define types of enterocyte clusters. Key and scale to the right. **(D)** FeaturePlot showing Ifne expression. Scale to the right. **(E)** FeaturePlot showing Ifnk expression split by Ifnε$^{-/-}$ and WT samples. Scale to the right.

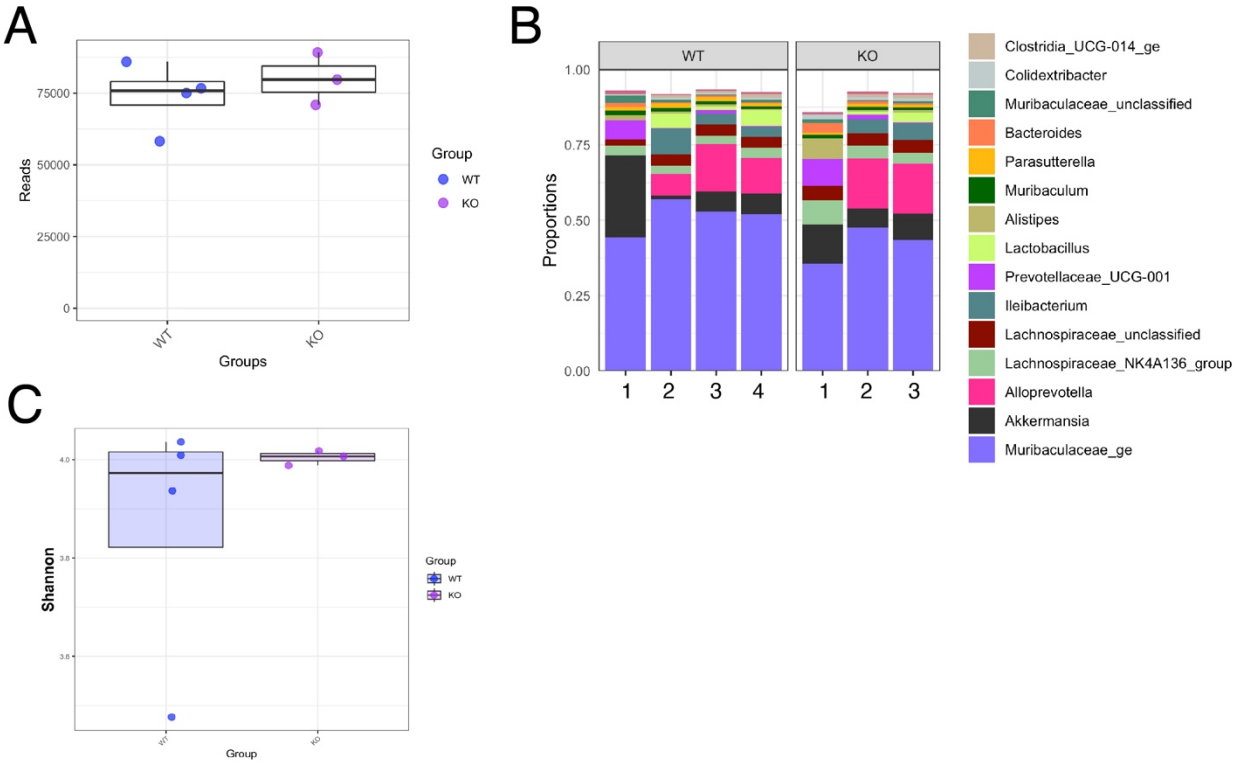

Supplemental Figure 9. (A), Total reads generated from 16S sequencing on fecal samples from *Ifn*$^{+/-}$ (WT) and *Ifnε*$^{-/-}$ (KO) littermates **(B),** Proportions of OTUs at each taxonomic rank in each sample **(C)** Alpha diversity measured by Shannon Index for *Ifnε*$^{+/-}$ (WT) and *Ifnε*$^{-/-}$ (KO) littermates.

Literature Cited

Beumer, J., J. Puschhof, F.Y. Yengej, L. Zhao, A. Martinez-Silgado, M. Blotenburg, H. Begthel, C. Boot, A. van Oudenaarden, Y.G. Chen, and H. Clevers. 2022. BMP gradient along the intestinal villus axis controls zonated enterocyte and goblet cell states. *Cell Rep* 38:110438.

Bourke, N.M., S.L. Achilles, S.U. Huang, H.E. Cumming, S.S. Lim, I. Papageorgiou, L.J. Gearing, R. Chapman, S. Thakore, N.E. Mangan, S. Mesiano, and P.J. Hertzog. 2022. Spatiotemporal regulation of human IFN-epsilon and innate immunity in the female reproductive tract. *JCI Insight* 7:

Burclaff, J., R.J. Bliton, K.A. Breau, M.T. Ok, I. Gomez-Martinez, J.S. Ranek, A.P. Bhatt, J.E. Purvis, J.T. Woosley, and S.T. Magness. 2022. A Proximal-to-Distal Survey of Healthy Adult Human Small Intestine and Colon Epithelium by Single-Cell Transcriptomics. *Cell Mol Gastroenterol Hepatol* 13:1554-1589.

Byers, S.L., M.V. Wiles, S.L. Dunn, and R.A. Taft. 2012. Mouse estrous cycle identification tool and images. *PLoS One* 7:e35538.

Coldbeck-Shackley, R.C., O. Romeo, S. Rosli, L.J. Gearing, J.A. Gould, S.S. Lim, K.H. Van der Hoek, N.S. Eyre, B. Shue, S.A. Robertson, S.M. Best, M.D. Tate, P.J. Hertzog, and M.R. Beard. 2023. Constitutive expression and distinct properties of IFN-epsilon protect the female reproductive tract from Zika virus infection. *PLoS Pathog* 19:e1010843.

de Geus, E.D., J.S. Volaric, A.Y. Matthews, N.E. Mangan, J. Chang, J.D. Ooi, N.A. de Weerd, E.M. Giles, and P.J. Hertzog. 2024. Epithelially Restricted Interferon Epsilon Protects Against Colitis. *Cell Mol Gastroenterol Hepatol* 17:267-278.

Demers, A., G. Kang, F. Ma, W. Lu, Z. Yuan, Y. Li, M. Lewis, E.N. Kraiselburd, L. Montaner, and Q. Li. 2014. The mucosal expression pattern of interferon-epsilon in rhesus macaques. *J Leukoc Biol* 96:1101-1107.

Deng, S., X. Tian, R. Belshaw, J. Zhou, S. Zhang, Y. Yang, C. Huang, W. Chen, H. Qiu, and S.W. Choo. 2024. An RNA-Seq analysis of coronavirus in the skin of the Pangolin. *Sci Rep* 14:910.

Fujii, M., M. Matano, K. Toshimitsu, A. Takano, Y. Mikami, S. Nishikori, S. Sugimoto, and T. Sato. 2018. Human Intestinal Organoids Maintain Self-Renewal Capacity and Cellular Diversity in Niche-Inspired Culture Condition. *Cell Stem Cell* 23:787-793 e786.

Fung, K.Y., E.D. de Geus, L. Ying, H. Cumming, N. Bourke, S.C. Foster, and P.J. Hertzog. 2024. Expression of Interferon Epsilon in Mucosal Epithelium is Regulated by Elf3. *Mol Cell Biol* 44:334-343.

Fung, K.Y., N.E. Mangan, H. Cumming, J.C. Horvat, J.R. Mayall, S.A. Stifter, N. De Weerd, L.C. Roisman, J. Rossjohn, S.A. Robertson, J.E. Schjenken, B. Parker, C.E. Gargett, H.P. Nguyen, D.J. Carr, P.M. Hansbro, and P.J. Hertzog. 2013. Interferon-epsilon protects the female reproductive tract from viral and bacterial infection. *Science* 339:1088-1092.

Garcia-Minambres, A., S.G. Eid, N.E. Mangan, C. Pade, S.S. Lim, A.Y. Matthews, N.A. de Weerd, P.J. Hertzog, and J. Mak. 2017. Interferon epsilon promotes HIV restriction at multiple steps of viral replication. *Immunol Cell Biol* 95:478-483.

Hafemeister, C., and R. Satija. 2019. Normalization and variance stabilization of single-cell RNA-seq data using regularized negative binomial regression. *Genome Biol* 20:296.

Hao, Y., T. Stuart, M.H. Kowalski, S. Choudhary, P. Hoffman, A. Hartman, A. Srivastava, G. Molla, S. Madad, C. Fernandez-Granda, and R. Satija. 2024. Dictionary learning for integrative, multimodal and scalable single-cell analysis. *Nat Biotechnol* 42:293-304.

Hardy, M.P., C.M. Owczarek, L.S. Jermiin, M. Ejdeback, and P.J. Hertzog. 2004. Characterization of the type I interferon locus and identification of novel genes. *Genomics* 84:331-345.

He, G.W., L. Lin, J. DeMartino, X. Zheng, N. Staliarova, T. Dayton, H. Begthel, W.J. van de Wetering, E. Bodewes, J. van Zon, S. Tans, C. Lopez-Iglesias, P.J. Peters, W. Wu, D. Kotlarz, C. Klein, T. Margaritis, F. Holstege, and H. Clevers. 2022. Optimized human intestinal organoid model reveals interleukin-22-dependency of paneth cell formation. *Cell Stem Cell* 29:1333-1345 e1336.

Jin, S. 2019. Bipotent stem cells support the cyclical regeneration of endometrial epithelium of the murine uterus. *Proc Natl Acad Sci U S A* 116:6848-6857.

Kellner, M.J., V.M. Monteil, P. Zelger, G. Pei, J. Jiao, M. Onji, K. Nayak, M. Zilbauer, A. Balkema-Buschmann, A. Dorhoi, A. Mirazimi, and J.M. Penninger. 2025. Bat organoids reveal antiviral responses at epithelial surfaces. *Nat Immunol* 26:934-946.

Korsunsky, I., N. Millard, J. Fan, K. Slowikowski, F. Zhang, K. Wei, Y. Baglaenko, M. Brenner, P.R. Loh, and S. Raychaudhuri. 2019. Fast, sensitive and accurate integration of single-cell data with Harmony. *Nat Methods* 16:1289-1296.

Kozich, J.J., S.L. Westcott, N.T. Baxter, S.K. Highlander, and P.D. Schloss. 2013. Development of a dual-index sequencing strategy and curation pipeline for analyzing amplicon sequence data on the MiSeq Illumina sequencing platform. *Appl Environ Microbiol* 79:5112-5120.

Lazear, H.M., J.W. Schoggins, and M.S. Diamond. 2019. Shared and Distinct Functions of Type I and Type III Interferons. *Immunity* 50:907-923.

Linderman, G.C., J. Zhao, M. Roulis, P. Bielecki, R.A. Flavell, B. Nadler, and Y. Kluger. 2022. Zero-preserving imputation of single-cell RNA-seq data. *Nat Commun* 13:192.

Love, M.I., W. Huber, and S. Anders. 2014. Moderated estimation of fold change and dispersion for RNA-seq data with DESeq2. *Genome Biol* 15:550.

Marks, Z.R.C., N. Campbell, N.A. deWeerd, S.S. Lim, L.J. Gearing, N.M. Bourke, and P.J. Hertzog. 2019. Properties and Functions of the Novel Type I Interferon Epsilon. *Semin Immunol* 43:101328.

Marks, Z.R.C., N.K. Campbell, N.E. Mangan, C.J. Vandenberg, L.J. Gearing, A.Y. Matthews, J.A. Gould, M.D. Tate, G. Wray-McCann, L. Ying, S. Rosli, N. Brockwell, B.S. Parker, S.S. Lim, M. Bilandzic, E.L. Christie, A.N. Stephens, E. de Geus, M.J. Wakefield, G.Y. Ho, O. McNally, S. Australian Ovarian Cancer, I.A. McNeish, D.D.L. Bowtell, N.A. de Weerd, C.L. Scott, N.M. Bourke, and P.J. Hertzog. 2023. Interferon-epsilon is a tumour suppressor and restricts ovarian cancer. *Nature* 620:1063-1070.

Martinez-Espinoza, I., P.I. Babawale, H. Miletello, N.R. Cheemarla, and A. Guerrero-Plata. 2024. Interferon Epsilon-Mediated Antiviral Activity Against Human Metapneumovirus and Respiratory Syncytial Virus. *Vaccines (Basel)* 12:

Matsumiya, T., S.M. Prescott, and D.M. Stafforini. 2007. IFN-epsilon mediates TNF-alpha-induced STAT1 phosphorylation and induction of retinoic acid-inducible gene-I in human cervical cancer cells. *J Immunol* 179:4542-4549.

Mayall, J.R., J.C. Horvat, N.E. Mangan, A. Chevalier, H. McCarthy, D. Hampsey, C. Donovan, A.C. Brown, A.Y. Matthews, N.A. de Weerd, E.D. de Geus, M.R. Starkey, R.Y. Kim, K. Daly, B.J. Goggins, S. Keely, S. Maltby, R. Baldwin, P.S. Foster, M.J. Boyle, P.S. Tanwar, N.D. Huntington, P.J. Hertzog, and P.M. Hansbro. 2024. Interferon-epsilon is a novel regulator of NK cell responses in the uterus. *EMBO Mol Med* 16:267-293.

McKie, A.T., D. Barrow, G.O. Latunde-Dada, A. Rolfs, G. Sager, E. Mudaly, M. Mudaly, C. Richardson, D. Barlow, A. Bomford, T.J. Peters, K.B. Raja, S. Shirali, M.A. Hediger, F. Farzaneh, and R.J. Simpson. 2001. An iron-regulated ferric reductase associated with the absorption of dietary iron. *Science* 291:1755-1759.

Miller, D., R. Romero, M. Kacerovsky, I. Musilova, J. Galaz, V. Garcia-Flores, Y. Xu, E. Pusod, C. Demery-Poulos, P. Gutierrez-Contreras, T.N. Liu, E. Jung, K.R. Theis, L.A. Coleman, and N. Gomez-Lopez. 2022. Defining a role for Interferon Epsilon in normal and complicated pregnancies. *Heliyon* 8:e09952.

1123 Moor, A.E., Y. Harnik, S. Ben-Moshe, E.E. Massasa, M. Rozenberg, R. Eilam, K. Bahar Halpern,
1124 and S. Itzkovitz. 2018. Spatial Reconstruction of Single Enterocytes Uncovers Broad
1125 Zonation along the Intestinal Villus Axis. *Cell* 175:1156-1167 e1115.
1126 Nguyen, N.K., E.C. Deehan, Z. Zhang, M. Jin, N. Baskota, M.E. Perez-Munoz, J. Cole, Y.E.
1127 Tuncil, B. Seethaler, T. Wang, M. Laville, N.M. Delzenne, S.C. Bischoff, B.R. Hamaker, I.
1128 Martinez, D. Knights, J.A. Bakal, C.M. Prado, and J. Walter. 2020. Gut microbiota
1129 modulation with long-chain corn bran arabinoxylan in adults with overweight and obesity
1130 is linked to an individualized temporal increase in fecal propionate. *Microbiome* 8:118.
1131 Ohtsuka, M., M. Sato, H. Miura, S. Takabayashi, M. Matsuyama, T. Koyano, N. Arifin, S.
1132 Nakamura, K. Wada, and C.B. Gurumurthy. 2018. i-GONAD: a robust method for in situ
1133 germline genome engineering using CRISPR nucleases. *Genome Biol* 19:25.
1134 Pleguezuelos-Manzano, C., J. Puschhof, S. van den Brink, V. Geurts, J. Beumer, and H.
1135 Clevers. 2020. Establishment and Culture of Human Intestinal Organoids Derived from
1136 Adult Stem Cells. *Curr Protoc Immunol* 130:e106.
1137 Robinson, C.M., M.A. Woods Acevedo, B.T. McCune, and J.K. Pfeiffer. 2019. Related Enteric
1138 Viruses Have Different Requirements for Host Microbiota in Mice. *J Virol* 93:
1139 Satija, R., J.A. Farrell, D. Gennert, A.F. Schier, and A. Regev. 2015. Spatial reconstruction of
1140 single-cell gene expression data. *Nat Biotechnol* 33:495-502.
1141 Schloss, P.D., S.L. Westcott, T. Ryabin, J.R. Hall, M. Hartmann, E.B. Hollister, R.A. Lesniewski,
1142 B.B. Oakley, D.H. Parks, C.J. Robinson, J.W. Sahl, B. Stres, G.G. Thallinger, D.J. Van
1143 Horn, and C.F. Weber. 2009. Introducing mothur: open-source, platform-independent,
1144 community-supported software for describing and comparing microbial communities.
1145 *Appl Environ Microbiol* 75:7537-7541.
1146 Skavicus, S., and N.S. Heaton. 2023. Approaches for timeline reductions in pathogenesis
1147 studies using genetically modified mice. *Microbiol Spectr* 11:e0252123.
1148 Stifter, S.A., A.Y. Matthews, N.E. Mangan, K.Y. Fung, A. Drew, M.D. Tate, T.P. Soares da Costa,
1149 D. Hampsey, J. Mayall, P.M. Hansbro, A. Garcia Minambres, S.G. Eid, J. Mak, J. Scoble,
1150 G. Lovrecz, N.A. deWeerd, and P.J. Hertzog. 2018. Defining the distinct, intrinsic
1151 properties of the novel type I interferon, IFNϵ. *J Biol Chem* 293:3168-3179.
1152 Triana, S., M.L. Stanifer, C. Metz-Zumaran, M. Shahraz, M. Mukenhirn, C. Kee, C. Serger, R.
1153 Koschny, D. Ordonez-Rueda, M. Paulsen, V. Benes, S. Boulant, and T. Alexandrov.
1154 2021. Single-cell transcriptomics reveals immune response of intestinal cell types to viral
1155 infection. *Mol Syst Biol* 17:e9833.
1156 Van Winkle, J.A., S.T. Peterson, E.A. Kennedy, M.J. Wheadon, H. Ingle, C. Desai, R. Rodgers,
1157 D.A. Constant, A.P. Wright, L. Li, M.N. Artyomov, S. Lee, M.T. Baldridge, and T.J. Nice.
1158 2022. Homeostatic interferon-lambda response to bacterial microbiota stimulates
1159 preemptive antiviral defense within discrete pockets of intestinal epithelium. *Elife* 11:
1160 Wang, Y., W. Song, J. Wang, T. Wang, X. Xiong, Z. Qi, W. Fu, X. Yang, and Y.G. Chen. 2020.
1161 Single-cell transcriptome analysis reveals differential nutrient absorption functions in
1162 human intestine. *J Exp Med* 217:
1163 Wijayarathna, R., E.D. de Geus, R. Genovese, L.J. Gearing, G. Wray-McCann, R. Sreenivasan,
1164 H. Hasan, M. Fijak, P. Stanton, D. Fietz, A. Pilatz, H.C. Schuppe, M.D. Tate, P.J.
1165 Hertzog, and M.P. Hedger. 2024. Interferon epsilon is produced in the testis and protects
1166 the male reproductive tract against virus infection, inflammation and damage. *PLoS*
1167 *Pathog* 20:e1012702.
1168 Winkler, I., A. Tolkachov, F. Lammers, P. Lacour, K. Daugelaite, N. Schneider, M.L. Koch, J.
1169 Panten, F. Grunschlager, T. Poth, B.M. Avila, A. Schneider, S. Haas, D.T. Odom, and A.
1170 Goncalves. 2024. The cycling and aging mouse female reproductive tract at single-cell
1171 resolution. *Cell* 187:981-998 e925.
1172